Figure 6.35: Cross sections of Cable 3 at maximum crushing load; at left, experimental test; at right, 2D FE model.

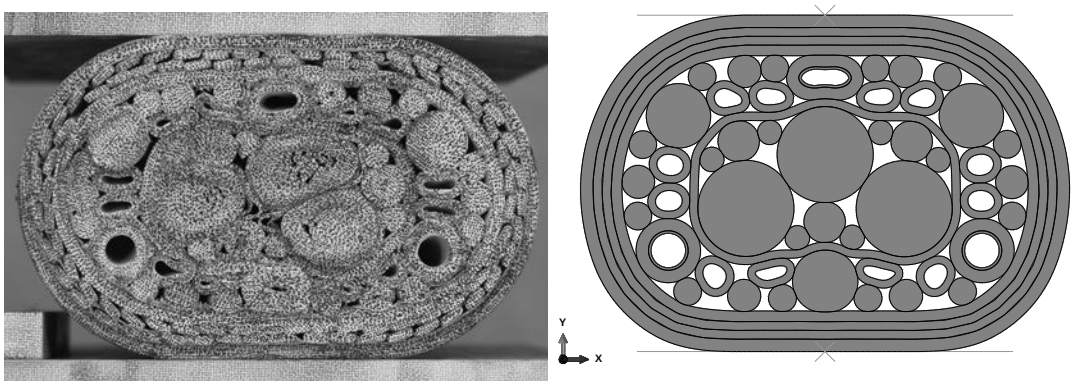

6.4 DISPLACEMENT FIELD ASSESSMENTS

The results presented in the previous section concerned only force-displacement standard measurements. However, as described in the beginning of this chapter, the whole experimental campaign was recorded with a DIC system. In this section, DIC results from the tests with the HCR-hoses umbilicals and Cables 2 and 3 are used to assess certain displacement fields. These experimental results are directly correlated with the displacement fields obtained from the numerical in-plane models. It should be noted that: 1) some preliminary analyses were conducted to establish an experimental methodology capable of monitoring the integrity of the tubular components; and 2) the DIC was used to assess displacement fields only, but not strain fields. As the umbilical cross sections are composed of several different components and do not present a continuous surface, it would be theoretically inappropriate to evaluate strain fields of the whole sections. For this reason, the experimental analysis herein developed is completely based on displacement measurements.

Concerning the 2D FE model of Cable 2, Figure 6.36 illustrates the displacement field for the horizontal component and Figure 6.37 shows the displacement field for the vertical component. Both results were obtained for a load per unit length (since it is a 2D model) of $50N/mm$, the same maximum load applied experimentally. The symmetry in the displacement fields is rather noticeable and is due to the configuration of the umbilical cross section and the crushing load.

For Cable 3, Figure 6.38 and Figure 6.39 present the corresponding displacement fields for horizontal and vertical components. These results correspond to a crushing load of $33N/mm$, the same maximum load applied in the experimental tests for this cable. Following the procedures previously described in this chapter, these load limits were set to avoid any plastic strain in the FE simulations.

Figure 6.40 and Figure 6.41 on the next page illustrate the vertical and horizontal displace-

Figure 6.36: Cable 2. Horizontal displacement field (mm) obtained with the 2D FE methodology; crushing load at $50N/mm$.

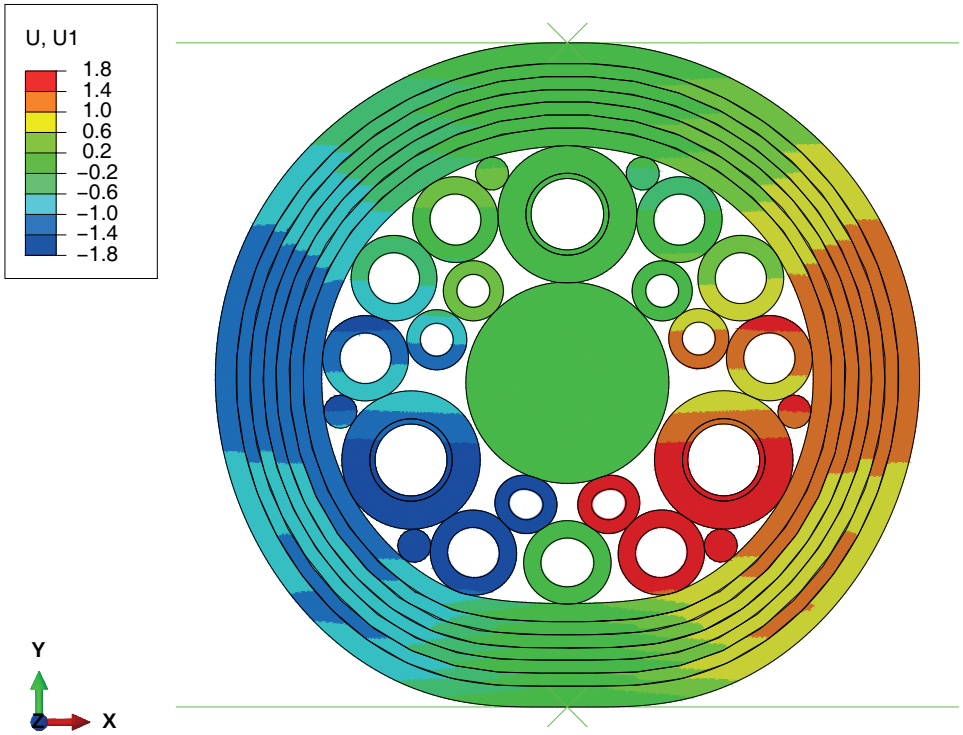

Figure 6.37: Cable 2. Vertical displacement field (mm) obtained with the 2D FE methodology, crushing load at $50N/mm$.

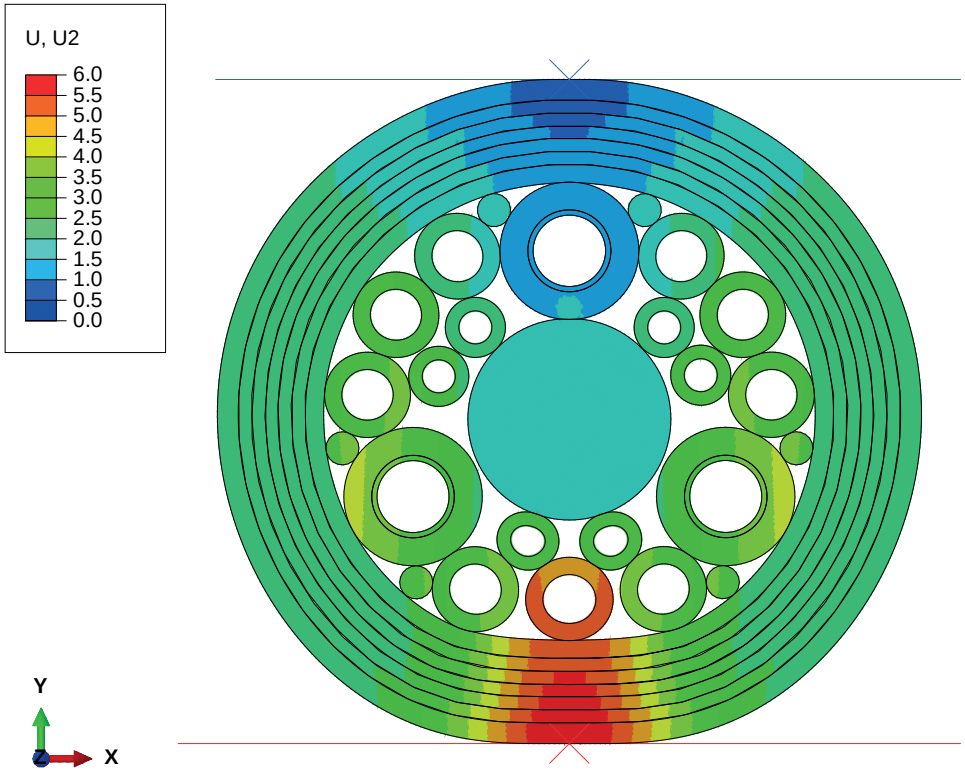

Figure 6.38: Cable 3. Horizontal displacement field (mm) obtained with the 2D FE methodology, crushing load at $33N/mm$.

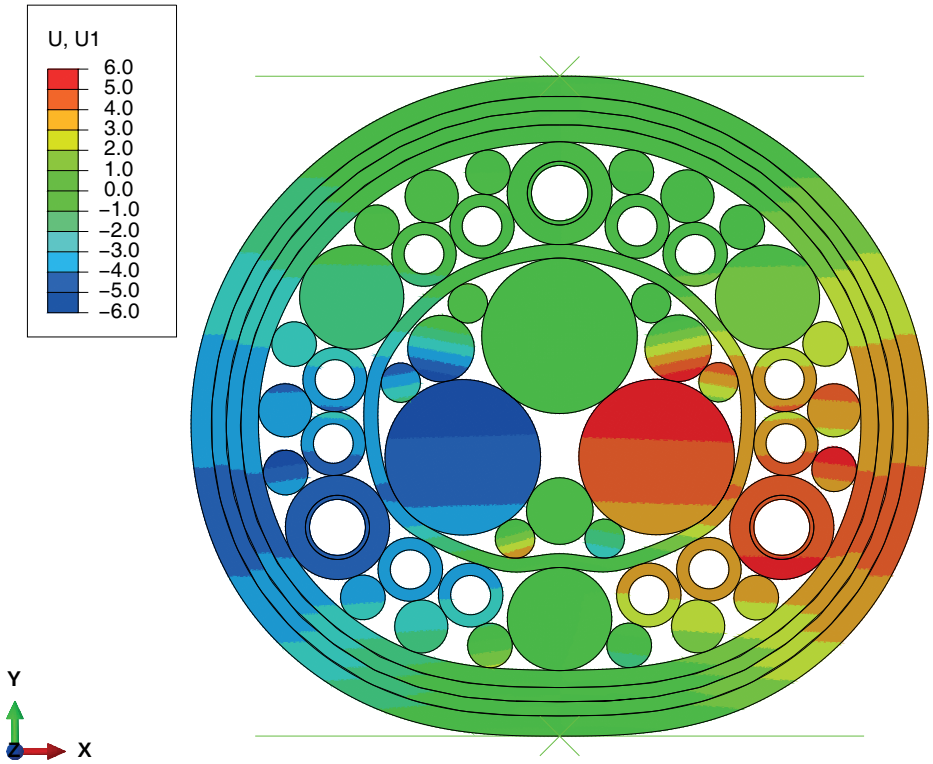

Figure 6.39: Cable 3. Vertical displacement field (mm) obtained with the 2D FE methodology, crushing load at $33N/mm$.

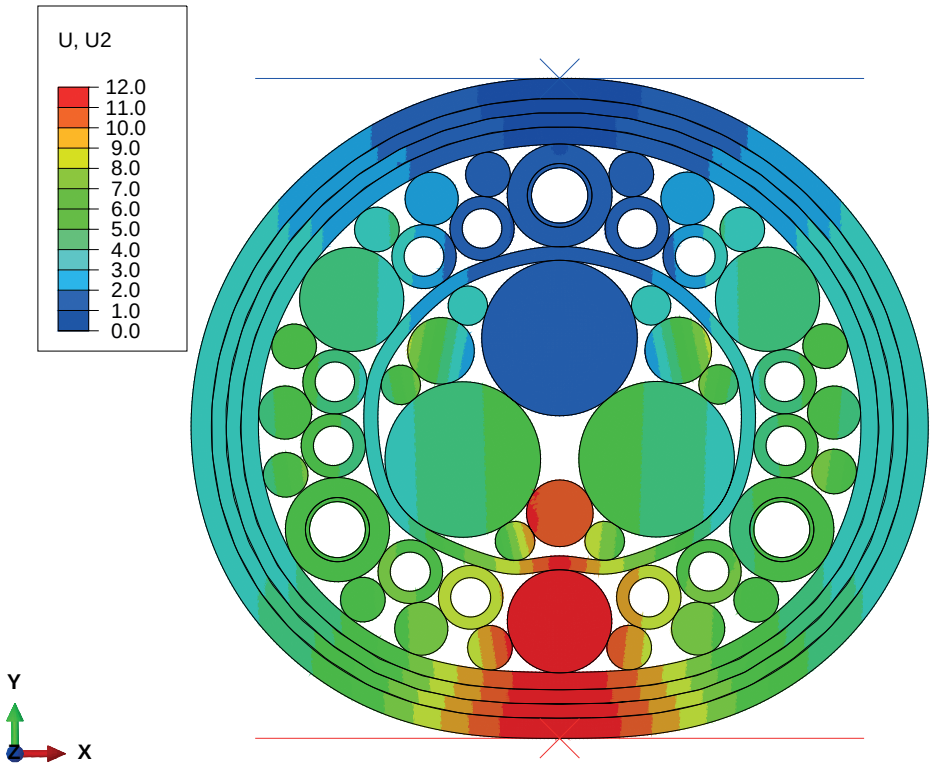

ment fields obtained with the DIC system, for Cable 2 in positions A through F. As for the numerical results, the displacement fields are measured for the same loading condition. It is remarkable that the displacement field changes considerably with cable orientation. The cross section orientation influences significantly the distribution of loads over the components: regions near fillers and thermoplastic hoses have more than one color, indicating considerable deformation of these components, as would be expected. The HCR hoses, which show only one color, are stiffer.

The experimental displacement fields obtained with the DIC system are similar to the FE results shown in Figure 6.36 and Figure 6.37 for Cable 2. The differences in the displacement values are certainly due to component accommodations. Nevertheless, resultant fields from the numerical and experimental approaches resemble each other, except for two main differences:

- The lack of symmetry in the experimental results, certainly due to the components' pitch;
- The deformable electrical core, which is stiffer in the FE model.

In Figure 6.41, green regions predominate on the left of the cross section and the displacement field is not symmetric like the one obtained with the numerical results. This indicates that the components' pitch affects displacements in the experimental tests. The images also show that in the DIC measurements the core usually presented three different colors. The elements in the center do not act as a rigid body and the results indicate a deformation not predicted by the 2D model. In Figure 6.36 and Figure 6.37, the numerical displacement field presents a core with a nearly rigid-body motion. In fact, the equivalent core used in the ABAQUS simulation may be responsible for the higher radial stiffness predicted, when compared to the experimental results.

For Cable 3, Figure 6.42 and Figure 6.43 show the horizontal and vertical displacement fields measured with the DIC system. The displacement fields are also calculated for the compressed umbilical after some crushing cycles, and the cross section at the beginning of the test is used as the zero reference.

The electrical cables in the center of the cross section present quasi rigid-body motions. When the sample is crushed, these components present different colors, tending to separate horizontally in Figure 6.42.

The vertical displacement fields (Figure 6.43) are not symmetric, as in the DIC results with Cable 2. Nevertheless, as the hoses' pitch are reversed when compared with Cable 2, the trend in the results follows an inverse pattern. As can be seen in Figure 6.43, the components at the left side of the cross section present larger vertical displacements. The field obtained experimentally differs from the corresponding FE symmetrical results (Figure 6.39), emphasizing the role of three-dimensional pitch, which is not presented in the 2D

Figure 6.40: Cable 2. Horizontal displacement fields (mm) obtained with the DIC system. Crushing load of $50N/mm$ after 5 crushing load cycle. Orientations A to F.

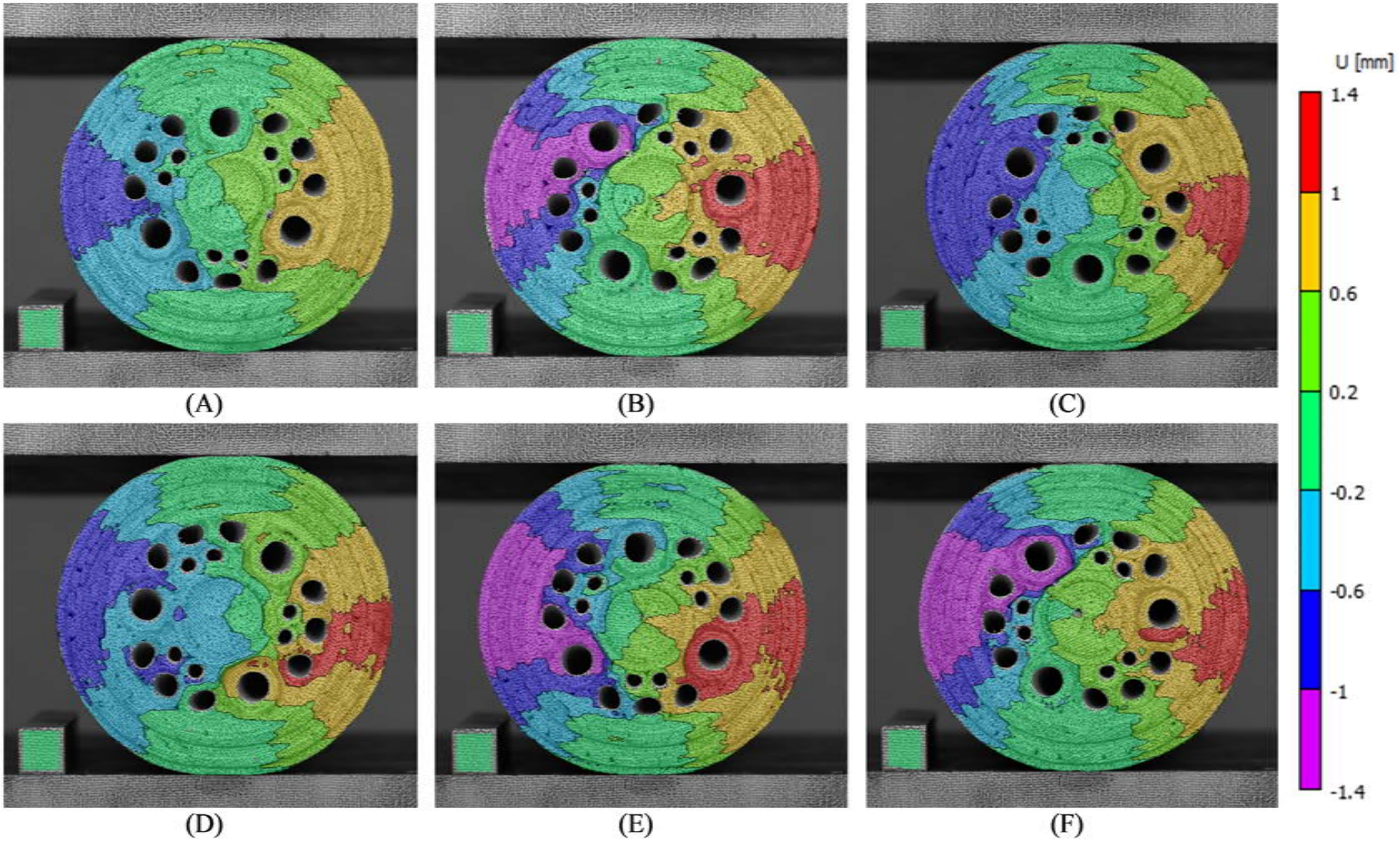

Figure 6.41: Cable 2. Vertical displacement fields (mm) obtained with the DIC system. Crushing load of $50N/mm$ after 5 crushing load cycle. Orientations A to F.

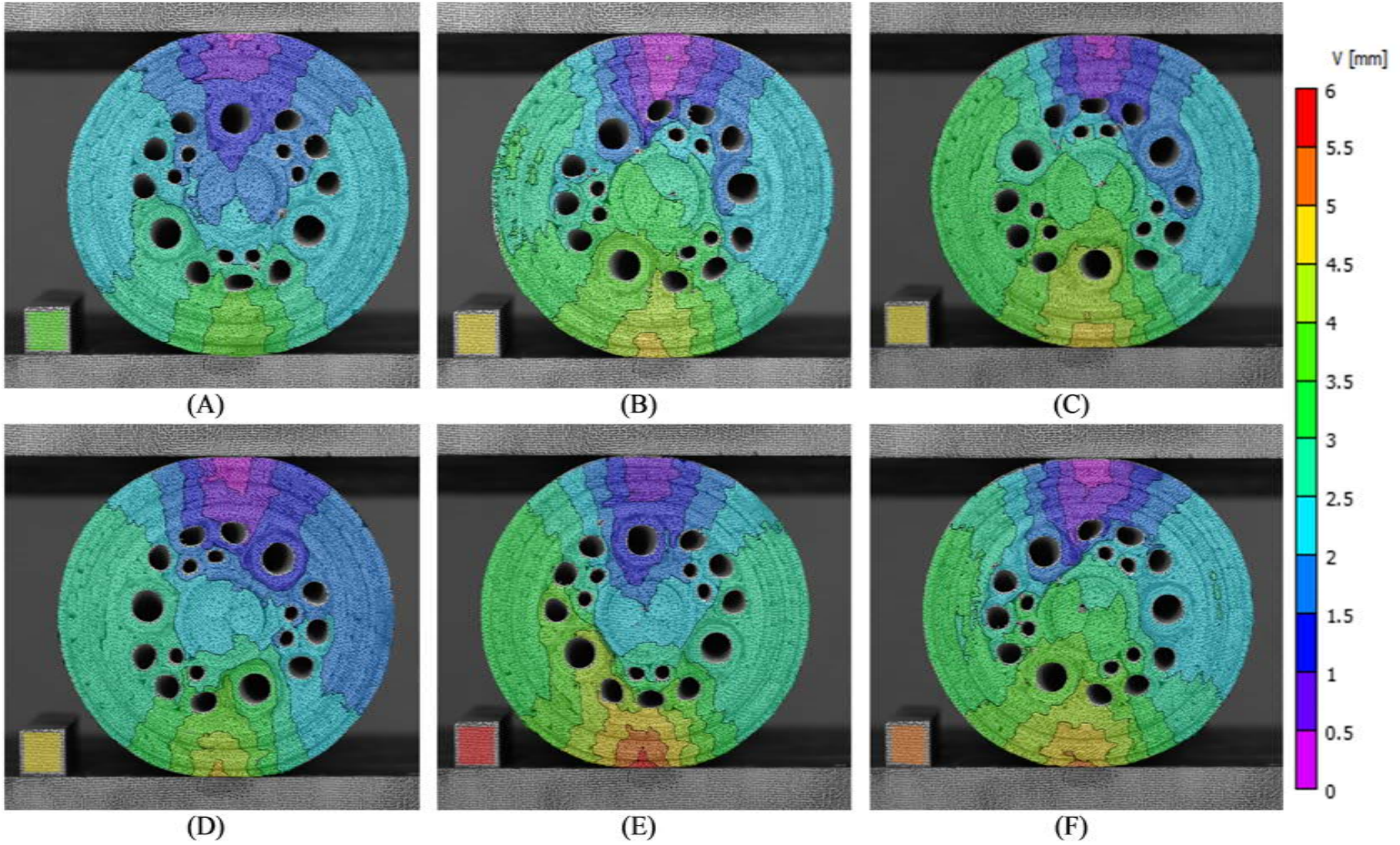

Figure 6.42: Cable 3. Horizontal displacement fields (mm) obtained with the DIC system. Crushing load of $33N/mm$• after 5 crushing load cycle. Orientations A to F.

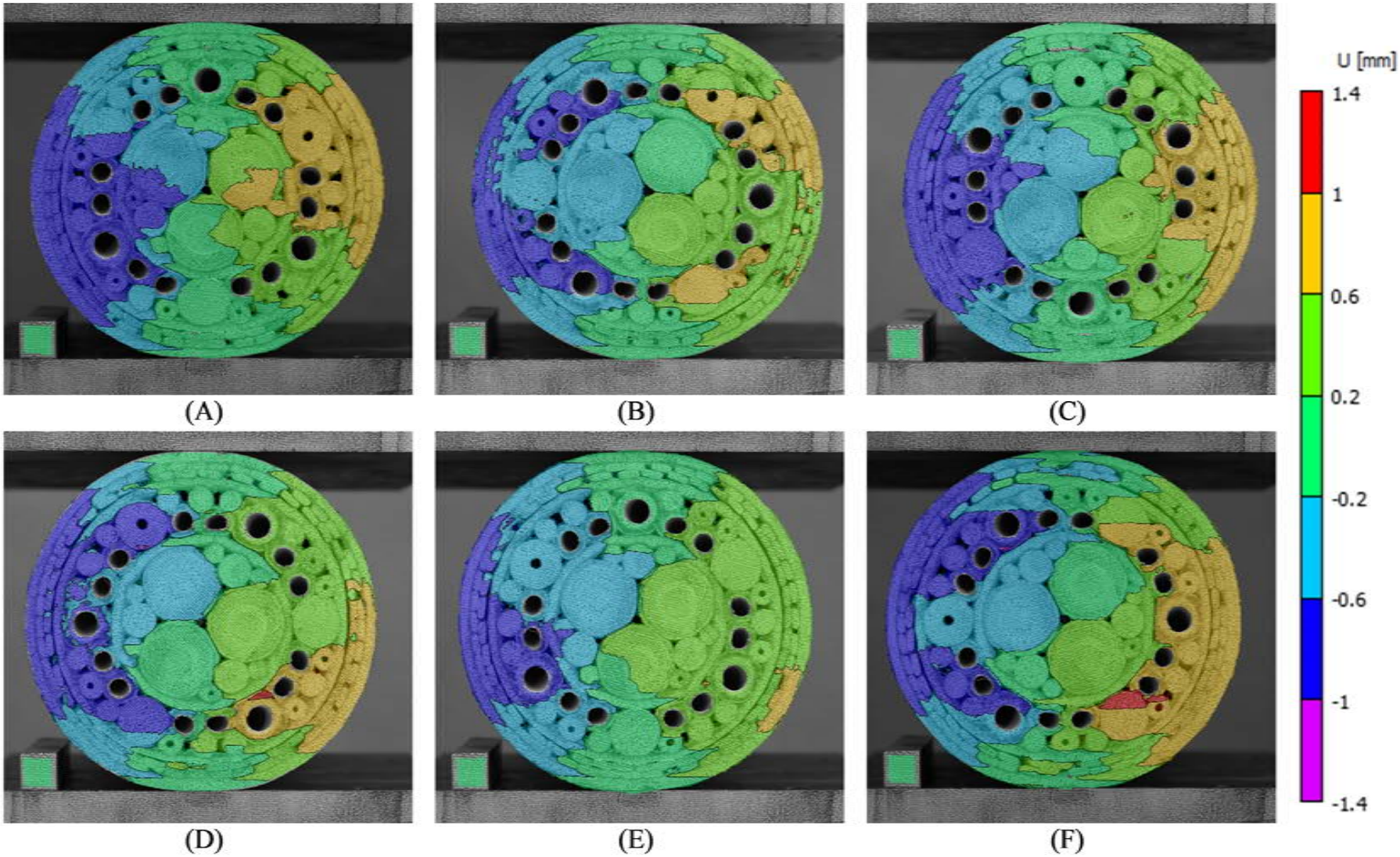

Figure 6.43: Cable 3. Vertical displacement fields (mm) obtained with the DIC system. Crushing load of $33N/mm$ after 5 crushing load cycle. Orientations A to F.

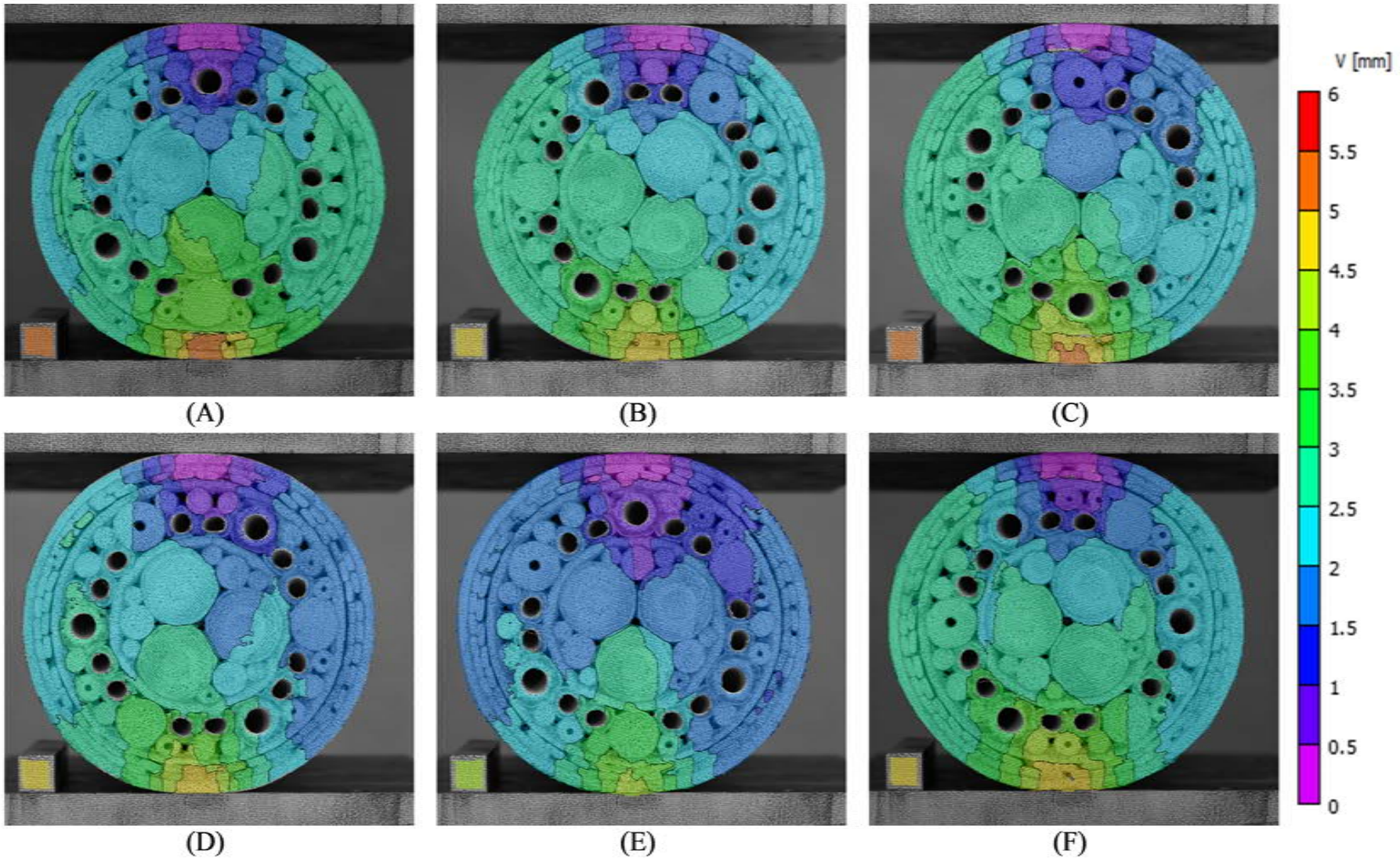

model. Once again, one should remember that the experimental measures are taken after five crushing load cycles, therefore after cumulative displacements.

6.5 CURVATURE TRACKING

The DIC system is conventionally used to obtain field results, as described in the previous section; however, the experimental assessment herein presented is not interested in displacement or strain fields. To analyze the integrity of the tubular components in the umbilical cross section, the DIC system is used here to detect how the profiles of these tubes and hoses are modified throughout the tests. By calculating the curvature of these profiles during each test, it is possible to quantify how these internal components are redistributing the crushing load from the shoes. The 'high-loading' experimental cases presented in Section 6.3 were analyzed with this new approach. The same terminology to identify specimens and tests applies.

Another purpose of this innovative methodology of experimental analysis is to provide a comparison with the numerical FE models. Once the numerical models have been validated by the experimental results, they can be considered reliable and therefore apt to simulate actual conditions of a cable during its installation. In brief, a failure criteria was established, based on plastic hinge formation (kinking) and using the DIC measurements to feed a numerical in-plane model.

Figure 6.44 illustrates the presentation of the DIC system test results. The given examples are results from Test T1-08, with specimen C1-2. Once the displacement of each point of any profile is registered by the system during the test, the developed methodology performs a fitting function with a Fourier series, considering the first five terms of the series. The curvature along the profile is calculated using this fitting function.

The first image at the top left-handside illustrates the frontal cross section of the specimen captured by the DIC system camera. In red, the image highlights the external perimeter monitored by the system. The second image at the top shows the same monitored profile in the Cartesian system. In blue, the initial configuration of the profile at the beginning of the test. The dots indicate measurements obtained with the DIC system. Then, in red, the image gives the fitting curve of this profile with 5 terms of the Fourier series.

As previously mentioned, the curvature of the given profile is calculated with the derivatives of the Fourier series obtained during the test. The third image (top right) illustrates, in a polar diagram, the curvature results obtained. The same results are shown in the last image in the Cartesian system. To conclude, the image at the bottom left-handside presents the force-displacement diagram already known from previous results. The black curve is the same presented in Section 6.3 using conventional instrumentation to measure shoe displacement. In

Figure 6.44: Curvature tracking with the DIC system. Test T1-08 with specimen C1-2. Tracking of the external perimeter.

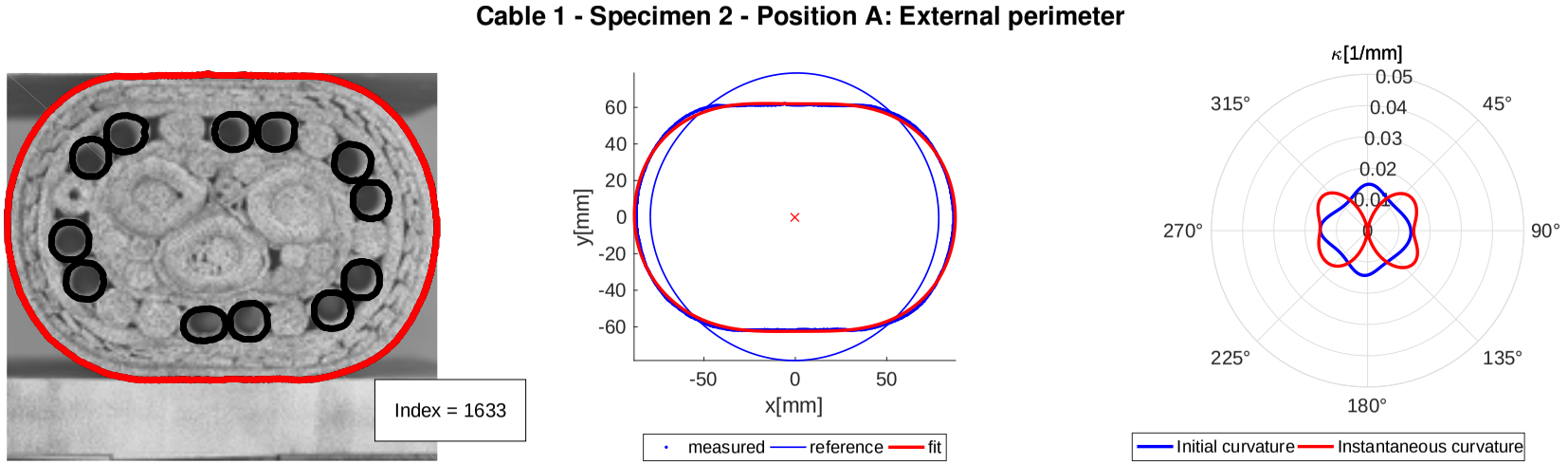

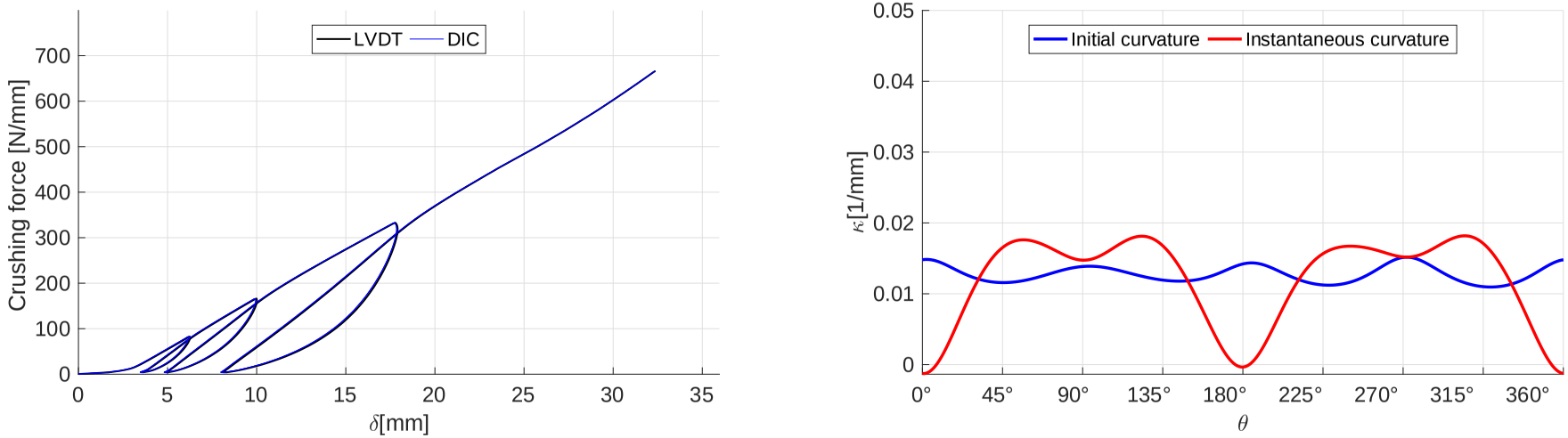

blue, the image presents the curve obtained using the vertical radius variation calculated with the DIC system. It is not difficult to see that the results are extremely consistent.

The following subsections present the DIC measurements in this same format. This experimental analysis covers the results from the 'high-loading' tests, which presented higher displacements.

6.5.1 Cable 1

The tubular components were labelled according to the terminology provided in Figure 6.45. The steel tubes of Cable 1 were numbered clockwise from 1 to 12. For each test, the DIC system tracked the tubular profiles and the outer perimeter of the cross section (in red).

This section presents results of the curvature obtained for the 'high-loading' tests with Cable 1. As the displacements and crushing forces are very high, there was unavoidable damage to the components.

With the DIC system constantly monitoring steel tubes, it is possible to get the maximum curvature presented during the tests for each component. Table 6.4 presents the results obtained for the three specimens of Cable 1. Red was used for the steel tube presenting the highest curvature.

Unfortunately, the DIC system malfunctioned and stopped monitoring halfway through the test with specimen C1-1. The test with specimen C1-3 did not present high curvature values. However, the curvature value for the test with specimen C1-2 exceeded $0.25mm^{-1}$, indicating that the crushing load was enough to crush the steel tubes. The tube that presented the highest deformation in Test T1-08 was Tube 12.

Figure 6.46 illustrates the results for Tube 12 obtained during test T1-08 (specimen C1-2) at the maximum crushing load. The umbilical cross section was visibly quite deformed. Nevertheless, most steel tubes' profiles in the monitored extremity did not suffer considerable deformations. The ones not aligned with the crushing load show no apparent deformation. Tube 12 (in red) underwent a visible deformation, certainly with yielding of the metallic thickness. The polar diagram at the top right illustrates the instantaneous curvature in red, while the graphic at the bottom right evaluates the curvature variation through the circumference of Tube 12.

According to the force vs. maximum curvature diagram at the bottom left of Figure 6.46, Tube 12 did not present significant deformation until a crushing load of about $450N/mm$ was reached. Beyond this point, the maximum curvature of the profile suddenly increases, indicating that the steel tube began to deform substantially. Before reaching $450N/mm$, the tube does not seem to be damaged. The load value corresponding to a sudden increase of

Figure 6.45: Enumerated tubes in the cross section of Cable 1 for identification during the DIC analysis.

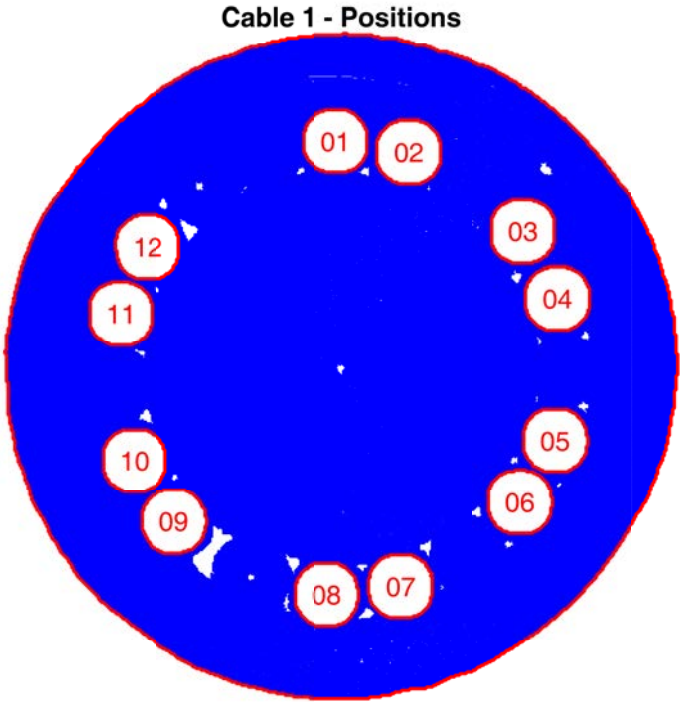

Table 6.4 : Maximum curvature for each hose obtained with the DIC system during the 'high-loading' tests. Tests T1-01, T1-08 and T1-15 were performed with all three specimens from Cable 1.

'High-loading' tests Maximum curvatures [1/mm]			
Specimen	**C1-1**	**C1-2**	**C1-3**
(Test ID)	*(T1-01)*	*(T1-08)*	*(T1-15)*
Tube 01	**0.168**	0.156	0.171
Tube 02	0.165	0.259	0.164
Tube 03	0.167	0.218	0.152
Tube 04	0.164	0.169	0.159
Tube 05	0.163	0.174	0.164
Tube 06	0.162	0.161	0.160
Tube 07	0.162	0.199	0.186
Tube 08	0.161	0.192	0.184
Tube 09	0.163	0.149	**0.187**
Tube 10	0.144	0.144	0.184
Tube 11	0.162	0.162	0.168
Tube 12	0.152	**0.263**	0.169

Figure 6.46: Curvature tracking with the DIC system. Test T1-08 with specimen C1-2. Tracking of Tube 12.

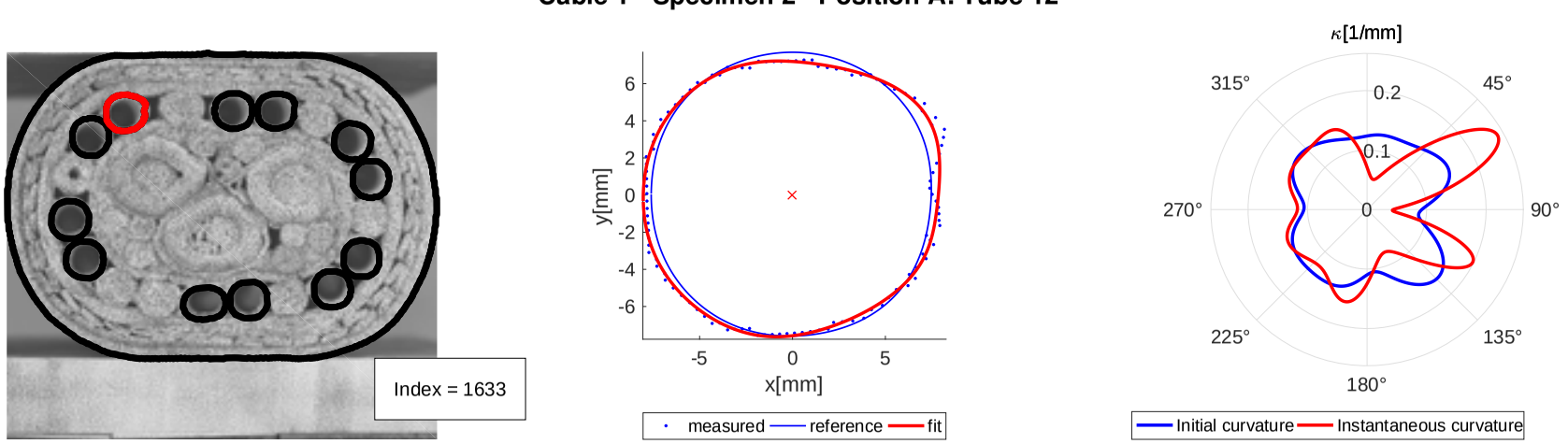

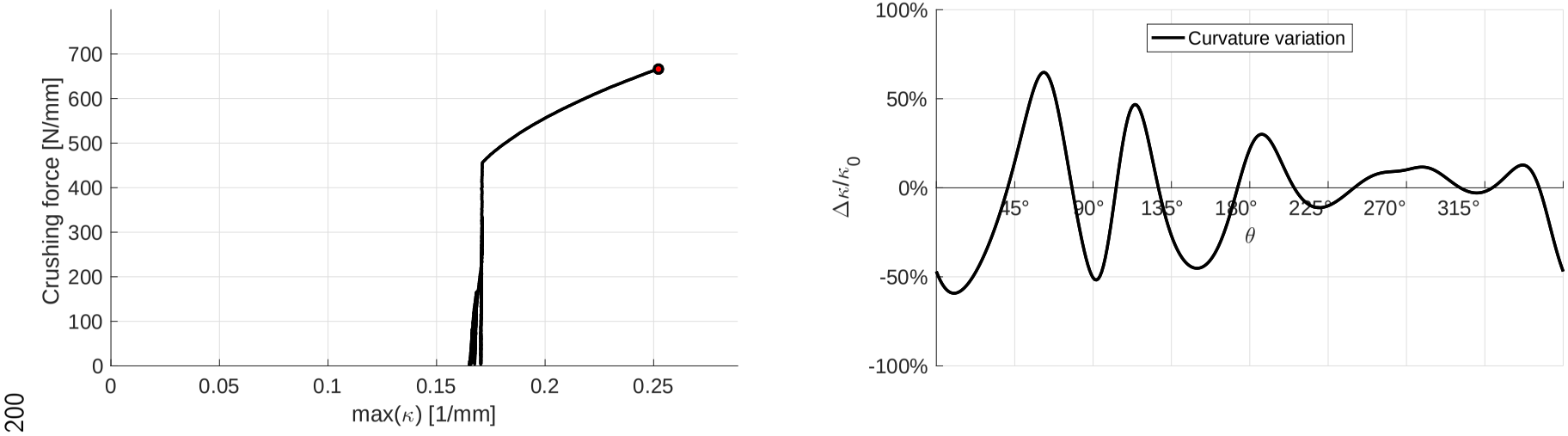

the maximum curvature along the tube perimeter is then proposed as a failure criterion, as follows.

To estimate the stress field in the metallic layer of this steel tube, a plane strain model of this component was designed in ABAQUS. A python script was implemented to use the DIC displacement measurements as inputs for a simple FEA of a single component. The rheology of the the metallic material is the same used in the previous chapter, considering elastic and plastic behaviors with a Ramberg-Osgood fitting. Displacements were imposed on the nodes of the internal perimeter, to recover the motions observed in the experimental test. This methodology made it possible to evaluate plastic strain through the section of the steel tube.

Results at 6 different moments of the analysis were enumerated and presented in Figure 6.47. Each column presents an evolution diagram of the crushing force vs. maximum curvature, the variation of the curvature through the perimeter and the magnitude of the plastic strain calculated numerically in the steel tube section. The first line illustrates the initial configuration. Line (2) identifies the moment when plastic strains higher than $0,2\%$ appear in the steel tube section. This value was taken arbitrarily as an elastoplastic threshold limit criterion, based on typical offset yield point criterion commonly adopted for tensile tests. Moment (3) indicates the moment previously mentioned, when the maximum curvature begins to increase considerably. It is worth noticing that this third moment almost coincides with the plastic hinge formation, which is depicted in the next line. The fourth line illustrates the formation of two plastic hinges in the profile of the steel tube, around $0°$ and $45°$. The subsequent line illustrates the results obtained at the maximum crushing force. The plastic strain field obtained with the FE model coincides with the calculation of the curvature variation. Peaks in the curvature variation diagram can be identified with green and red colors in the FE strain field. The maximum plastic strain reached at around $45°$ was 8%. Finally, the last line illustrates the curvature variation and the corresponding residual plastic strain field after unloading. For this case, the FE results obtained using the DIC measurements as inputs indicate an interdependence between the formation of plastic hinges in the profile of a metallic tube and the sudden increase in maximum curvature.

Figure 6.47: Evolution in six steps of the crushing load, curvature variation and plastic strain field; test T1-08 with specimen C1-2; results for Tube 12.

(1) Initial configuration;

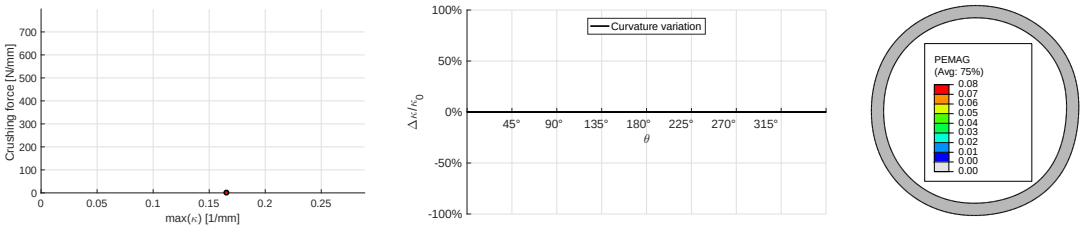

(2) First plastic strain in the metallic thickness (blue color indicates strains higher than 0.2%);

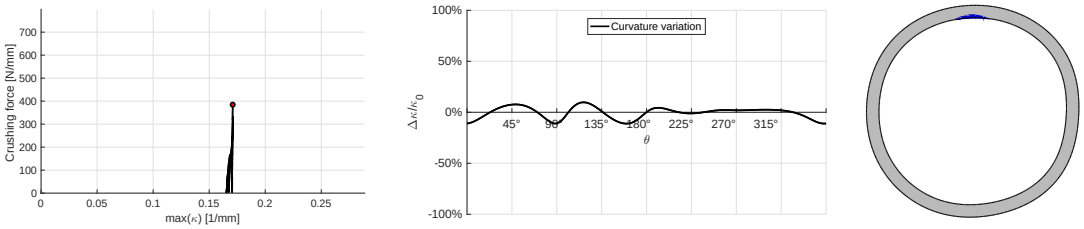

(3) Curvature variation begins to increase considerably;

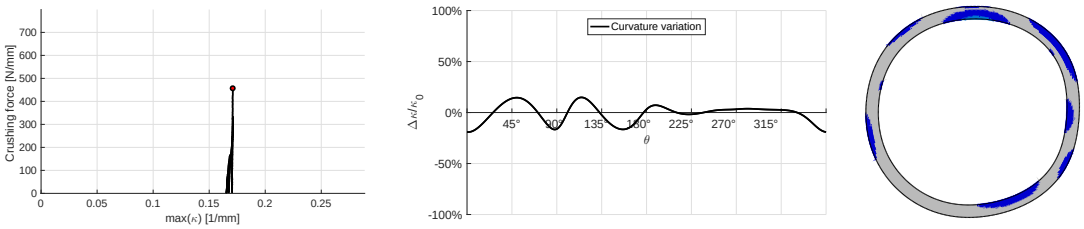

(4) Plastic hinge formation through the thickness;

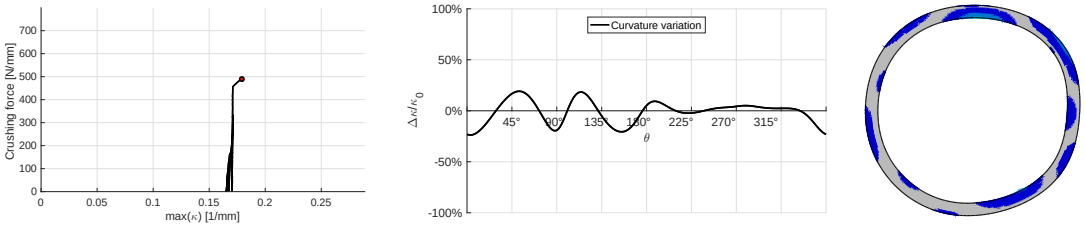

(5) Maximum crushing force;

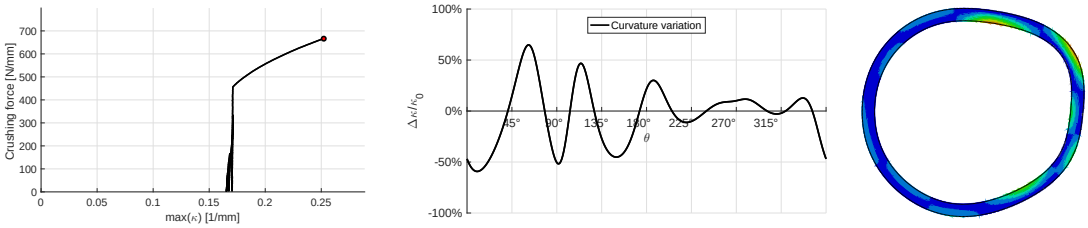

(6) Unloaded condition.

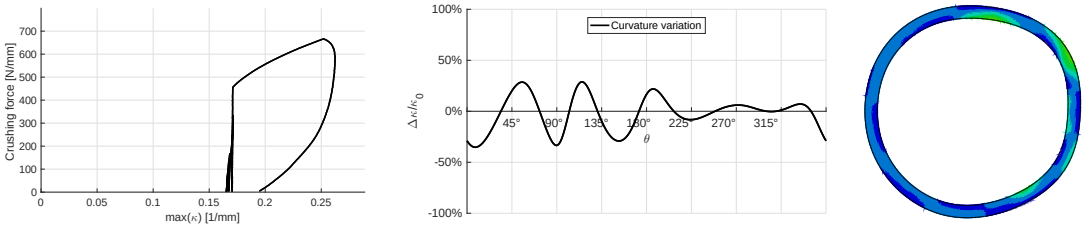

6.5.2 Cable 2

The same procedures were adopted for the experimental tests with Cable 2 specimens. Firstly, Figure 6.48 presents the terminology used to identify the components of the umbilical cross section. HCR and thermoplastic hoses are numbered clockwise from 1 to 12. Table 6.5 lists the maximum curvature reached by each element during the destructive crushing test.

Hose 01 showed the highest deformation in almost all crushing tests conducted with HCR hoses. This was expected, because during the 'high-loading' tests the specimens were crushed in Position A and Hose 01 was always aligned with the vertical crushing load.

One test was selected to exemplify the analysis. Figure 6.49 illustrates the result obtained for Test T2-17 (specimen C2-5). It is remarkable that the umbilical cross section was completely deformed. Some thermoplastic hoses were totally crushed. Nevertheless, the reinforced hoses did not suffer much. The HCR hoses not aligned with the crushing load did not show apparent deformation. However, Hose 01 underwent a visible deformation, with a noticeable yielding of the inner metallic carcass. The curvature variation exceeded 100% of the initial configuration value around $270°$ and $350°$.

Once again, it is important to draw attention to the diagram at the bottom left of Figure 6.49. Up to a crushing load of $340N/mm$, Hose 01 did not present a significant deformation. Beyond this point, the maximum curvature of the profile increases substantially, indicating a plastic failure of the carcass. Figure 6.50 illustrates the evolution of this load case, evaluating the stresses in Hose 01 using the same approach already described for Cable 1. The DIC displacement measurements were used as input for the plane strain FE model of a single element. In this case, as the geometry of the interlocked carcass cannot be reproduced in the 2D FE model, the same considerations adopted in the previous chapter were employed. The FE model was designed using an equivalent pipe (a ring in the in-plane model). It is worth remembering that the equivalent thickness was calculated according to Appendix D, to enable the recovery of the interlocked geometry's radial stiffness.

Figure 6.50 on page 206 depicts six steps of the experiment: the first line indicates the initial configuration of the HCR hose (Hose 1), with no curvature variation or plastic strain. The first plastic strain higher than 0.2% appeared around $270°$, when the curvature variation overcame 10%, regarding the corresponding initial value. Differently from the previous case, the third moment illustrated indicates the formation of plastic hinges that happens when the FE model evaluates a considerable plastic strain through the thickness of the equivalent pipe. The maximum curvature begins to increase in the fourth line, just after the plastic strain in practically all the perimeter gets higher than 0.2%. To complete the analysis, lines (5) and (6) indicate the moments at maximum crushing force and at the unloaded configuration,

Figure 6.48: Enumerated hoses in the cross section of Cable 2 for identification during the DIC analysis.

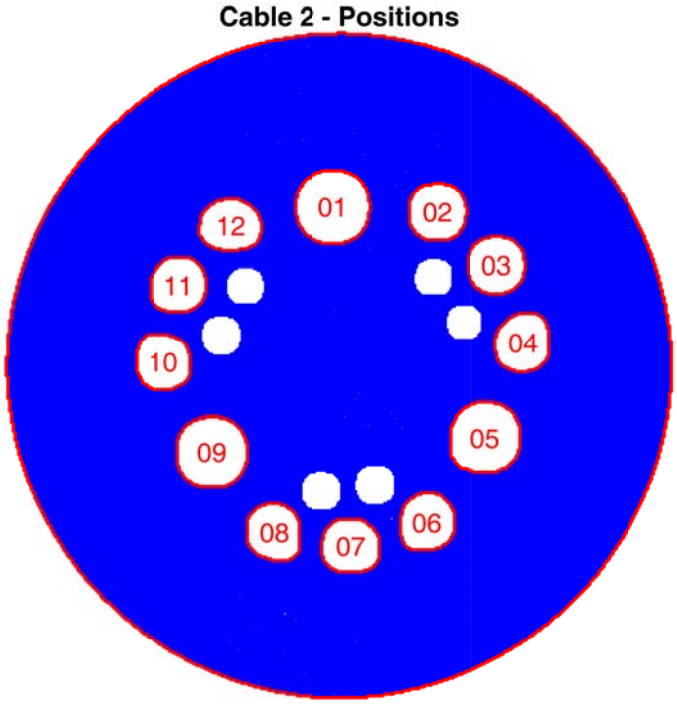

Table 6.5 : Maximum curvature for each hose obtained with the DIC system during the 'high-loading' tests. Tests T2-07, T2-08 and T2-15 to T2-18 performed with all six specimens of Cable 2.

'High-loading' tests Maximum curvatures [1/mm]							
Specimen *(Test ID)*		C2-1 *(T2-07)*	C2-2 *(T2-08)*	C2-3 *(T2-15)*	C2-4 *(T2-16)*	C2-5 *(T2-17)*	C2-7 *(T2-18)*
HCR hoses	Hose 01	0.189	**0.531**	**0.273**	**0.240**	**0.260**	**0.309**
	Hose 05	**0.207**	0.163	0.177	0.183	0.183	0.164
	Hose 09	0.172	0.180	0.164	0.175	0.166	0.188
Thermoplastic hoses	Hose 02	0.805	0.800	1.666	1.298	1.577	**2.862**
	Hose 03	1.154	1.858	1.145	1.535	1.071	1.211
	Hose 04	0.917	0.903	0.659	0.702	1.236	0.532
	Hose 06	1.121	1.494	2.627	2.004	2.336	0.593
	Hose 07	**6.222**	**4.804**	2.216	1.680	**4.265**	1.996
	Hose 08	1.022	0.905	1.268	1.335	1.598	2.478
	Hose 10	0.727	0.645	0.783	1.154	1.143	0.752
	Hose 11	0.688	1.460	1.066	1.291	3.350	1.298
	Hose 12	1.617	3.294	**3.164**	**3.901**	2.631	1.383

Figure 6.49: Curvature tracking with the DIC system. Test T2-17 with specimen C2-5. Tracking of Hose 01.

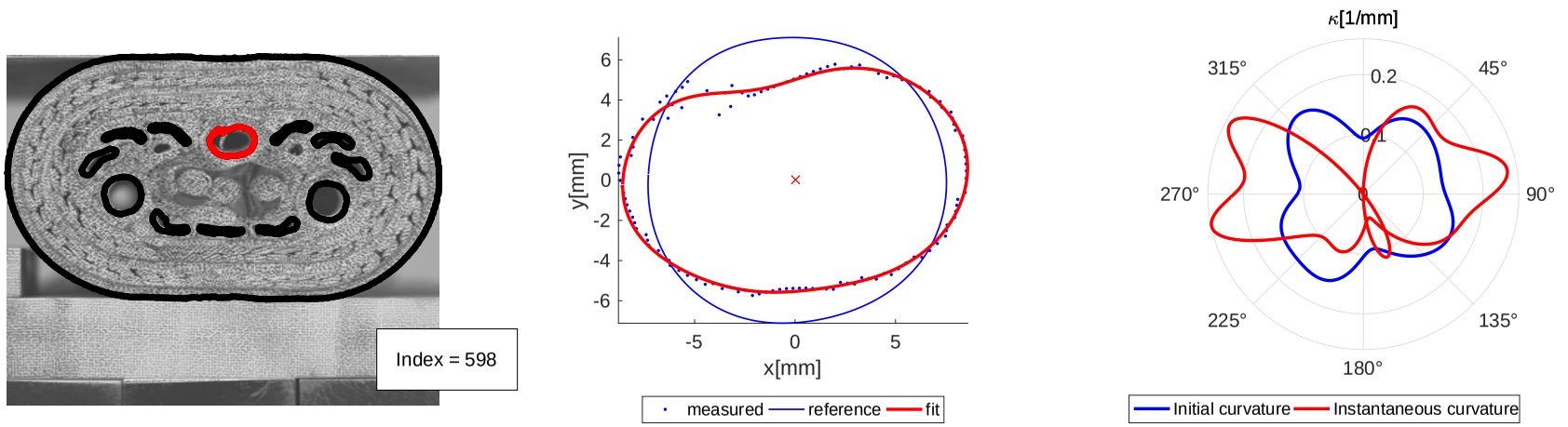

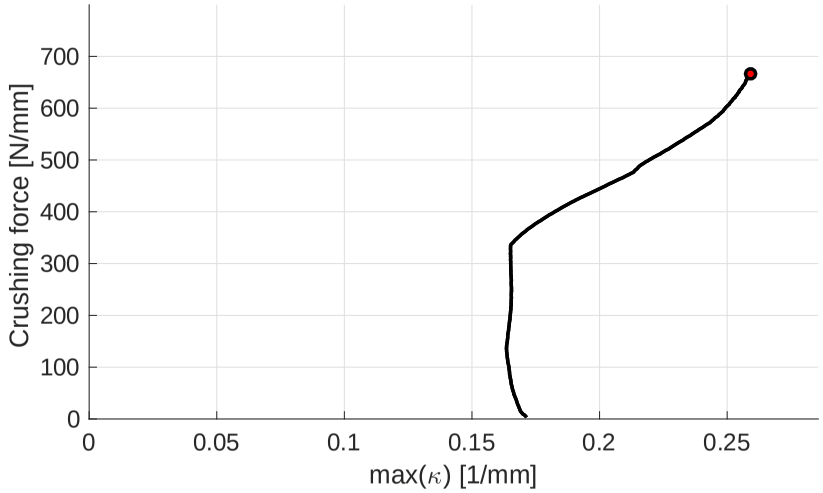

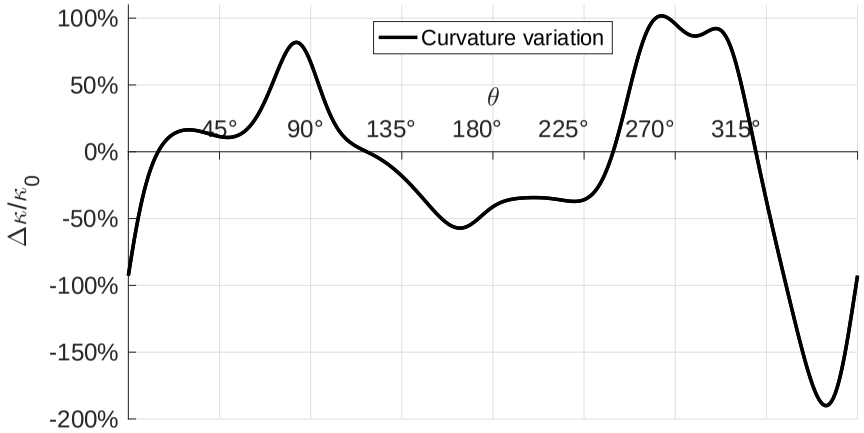

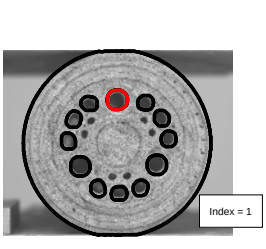

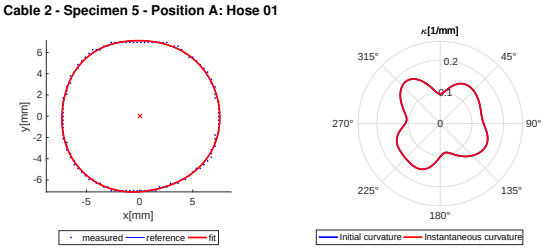

rain field; test T2-17

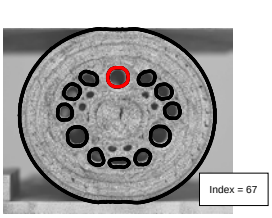

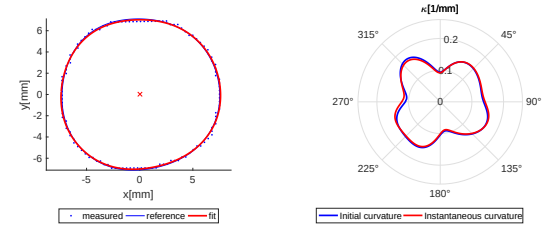

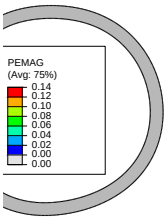

0.2%);

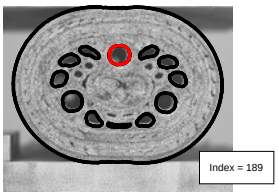

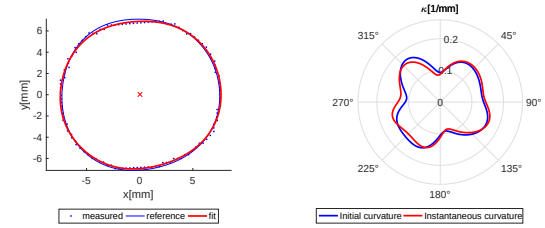

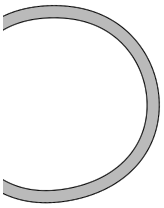

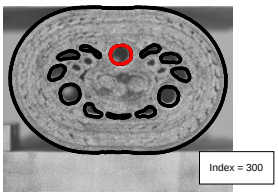

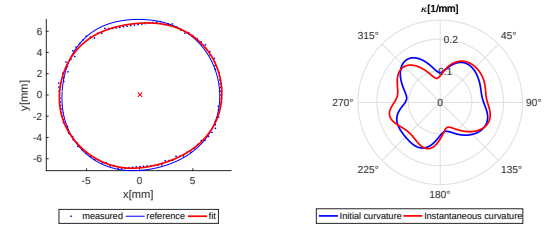

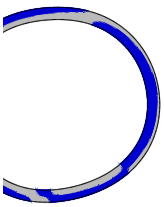

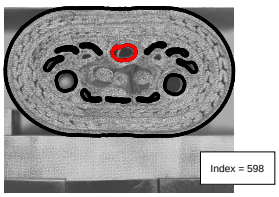

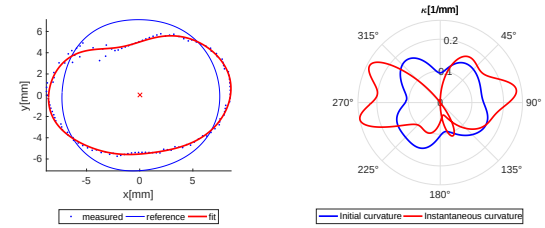

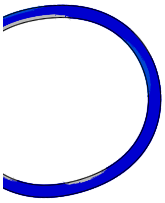

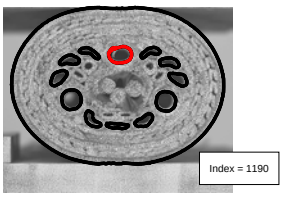

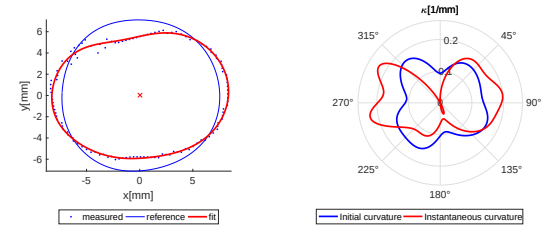

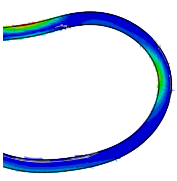

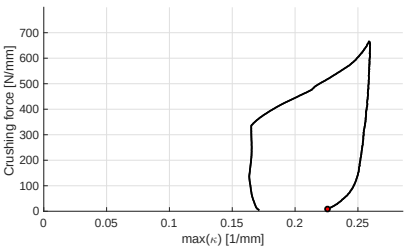

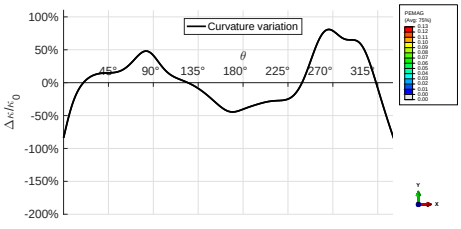

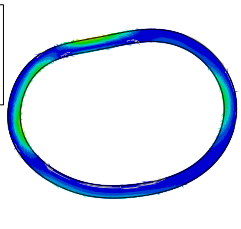

respectively. During the crushing test, the FE calculations indicated a maximum plastic strain of 14%. Typical mechanical properties of the 304L stainless steel indicate ultimate elongation values around 40%.

On the other hand, the displacements measured for the thermoplastic hoses during the 'high-loading' tests were more substantial. The obtained curvatures were at least ten times higher, as these hoses are more susceptible to deformation. As becomes evident by looking at Table 6.5, the most deformed thermoplastic hoses are those aligned with the load (Hoses 02, 07 and 12). Figure 6.51 illustrates the results of the DIC system for Test T2-17 (specimen C2-5), with the curvature analysis focusing on Hose 07.

Hose 07 presents a considerable increase in curvature, even for loads smaller than $100N/mm$. The curvature reaches a maximum at around $200N/mm$, indicating that this final deformed state shown in Figure 6.51 was reached with about 30% of the maximum crushing load.

Figure 6.51: Curvature tracking with the DIC system. Test T2-17 with specimen C2-5. Tracking of Hose 07

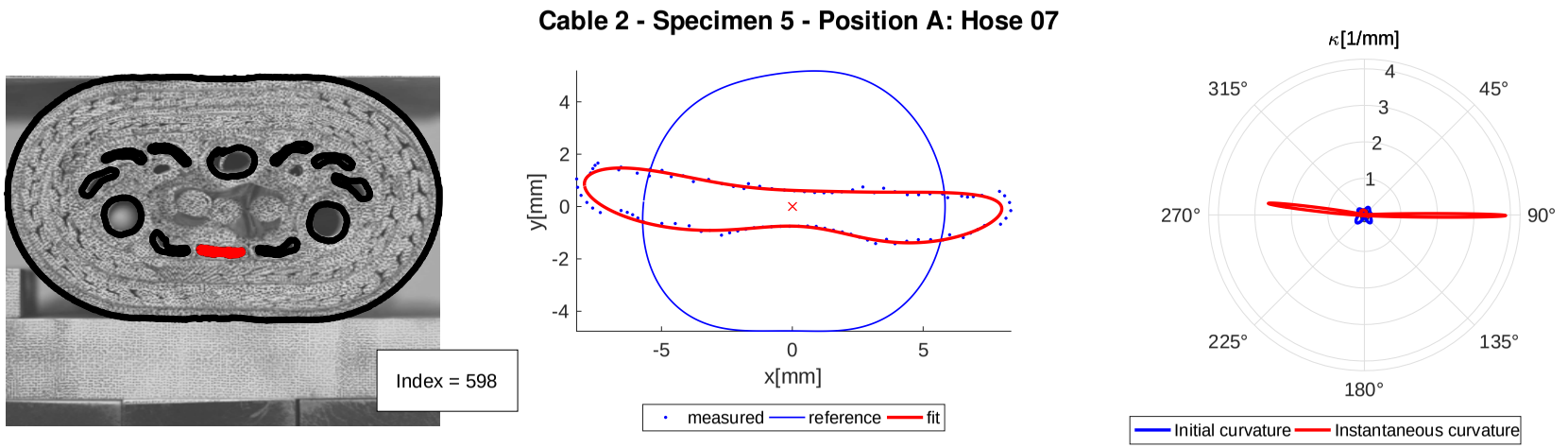

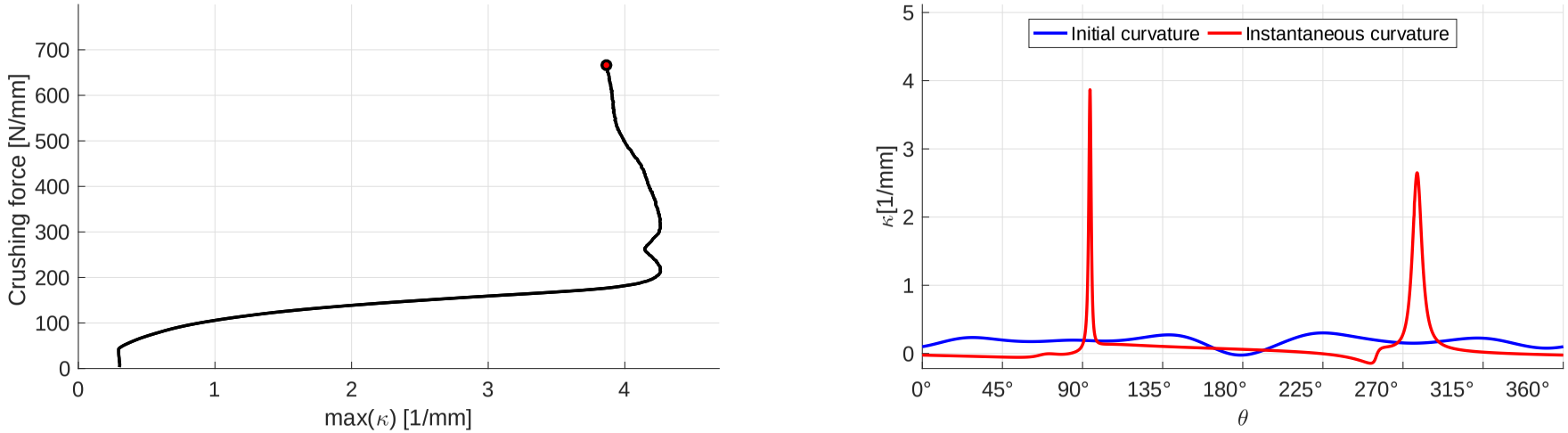

6.5.3 Cable 3

As for the previous DIC analyses with Cables 1 and 2, the hoses from Cable 3 were labeled as shown in Figure 6.52, with components numbered from 1 to 15. Table 6.6 summarizes the curvature results obtained during the destructive tests of the experimental campaign. Again, the curvature values indicate that the crushing loads were sufficient to crush the HCR hoses.

Among the crushed reinforced hoses, the one that showed the highest deformations was Hose 01, with the exception of Test T3-10. During the tests, Hose 01 was always aligned with the crushing load. In addition, for Test T3-10 with specimen C3-4, none of the HCR hoses seems to be substantially crushed.

To exemplify analysis one last time, Figure 6.53 illustrates results obtained for Test T3-01 (specimen C3-1). The force-curvature diagram at the bottom left presents again a bilinear character. Until a crushing load of about $200N/mm$, Hose 01 does not deform significantly. Beyond this point, the maximum curvature of the profile suddenly increases. The curvature variation approached 100% of the corresponding initial value at $180°$ and $270°$.

Figure 6.54 illustrates select moments of the experimental tests and the plastic strain field calculated through the plane strain FEA. Once again, it is possible to associate the abrupt raise in maximum curvature with the appearance of plastic hinges. The moments illustrated in lines (3) and (4) are very close in time.

Concerning thermoplastic hoses, higher curvatures can naturally be found. Figure 6.55 illustrates the DIC system results for Test T3-01 (specimen C3-1), with the curvatures of Hose 08. The images illustrate the unloaded moment. Even after unloading, Hose 8 presented a considerable increase in curvature.

Figure 6.52: Enumerated hoses for identification in the Cable 3 during the DIC analysis.

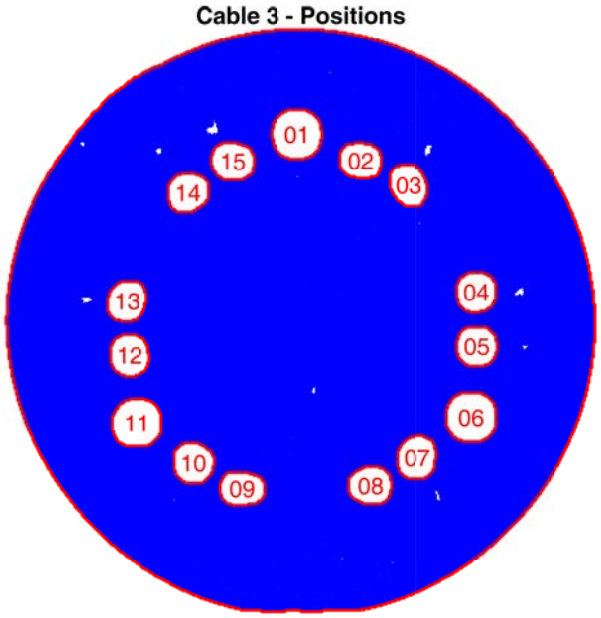

Table 6.6 : Maximum curvature for each hose obtained with the DIC system during the 'high-loading' tests. Tests T3-01 to T3-03, T3-10, T3-17 and T3-18 performed with all six specimens from Cable 3.

'High-loading' tests Maximum curvatures [1/mm]							
Specimen *(Test ID)*		C3-1 *(T3-01)*	C3-2 *(T3-02)*	C3-3 *(T3-03)*	C3-4 *(T3-10)*	C3-5 *(T3-17)*	C3-7 *(T3-18)*
HCR hoses	Hose 01	0.223	0.248	0.269	0.174	0.307	0.257
	Hose 06	0.170	0.150	0.171	0.171	0.144	0.166
	Hose 11	0.169	0.172	0.147	0.181	0.195	0.185
Thermoplastic hoses	Hose 02	0.633	1.553	5.037	1.293	0.460	0.803
	Hose 03	0.939	0.961	1.133	1.319	0.677	0.708
	Hose 04	0.416	0.398	0.820	0.442	0.485	0.446
	Hose 05	0.474	0.436	0.463	0.672	0.506	0.634
	Hose 07	1.110	0.984	1.831	0.983	1.246	0.863
	Hose 08	1.203	1.902	2.670	0.956	1.225	2.099
	Hose 09	1.124	0.617	0.905	0.740	0.980	1.052
	Hose 10	0.748	0.769	2.313	0.740	0.787	0.511
	Hose 12	0.294	0.563	0.518	0.529	0.443	0.512
	Hose 13	0.385	0.472	0.584	0.472	0.433	0.401
	Hose 14	0.583	1.073	1.322	0.884	0.952	1.007
	Hose 15	0.637	1.789	0.847	1.254	1.063	0.969

Figure 6.53: Curvature tracking with the DIC system. Test T3-01 with specimen C3-1. Tracking of Hose 01.

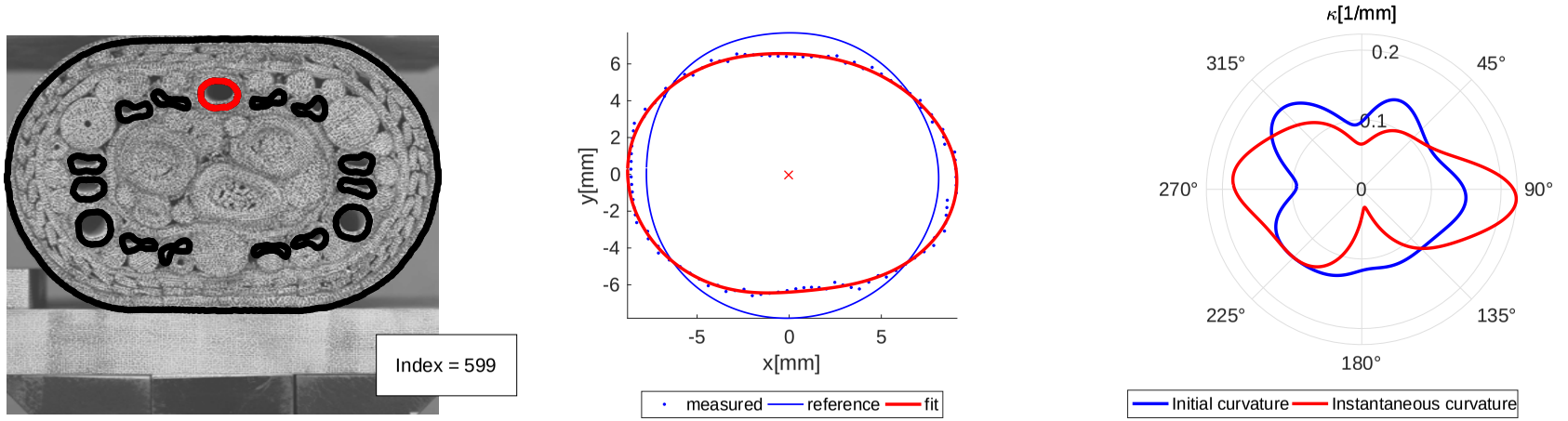

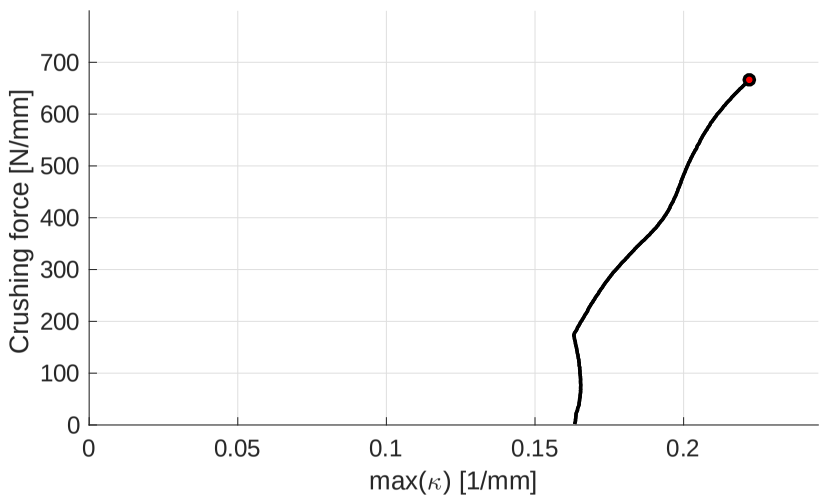

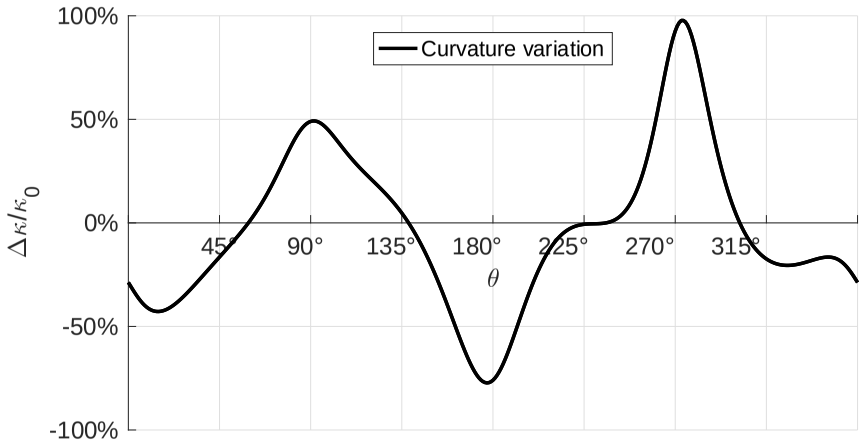

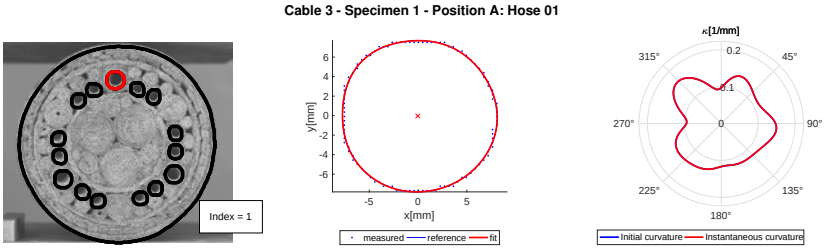

rain field; test T3-01

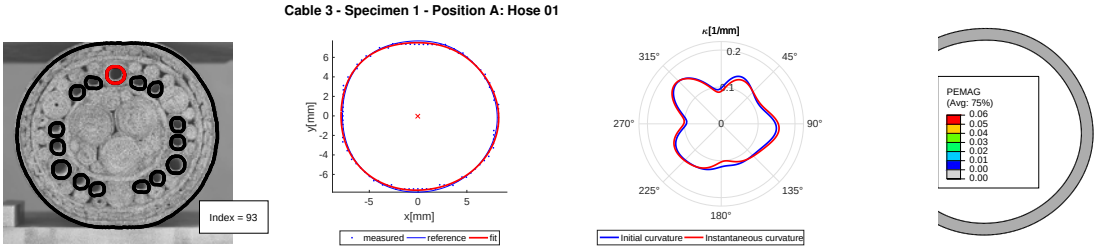

0.2%);

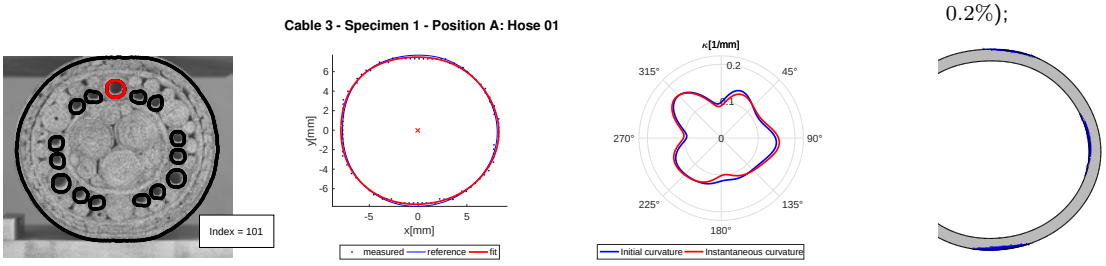

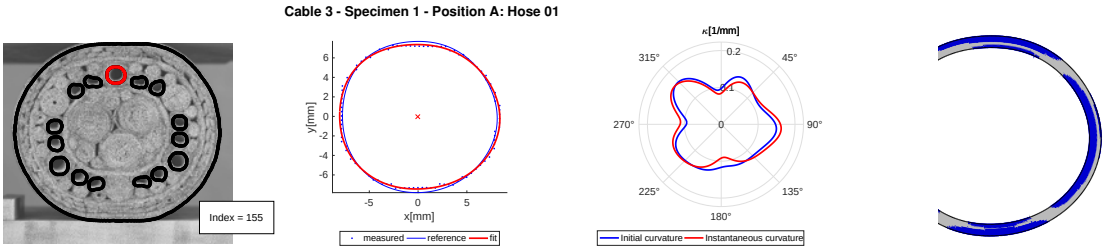

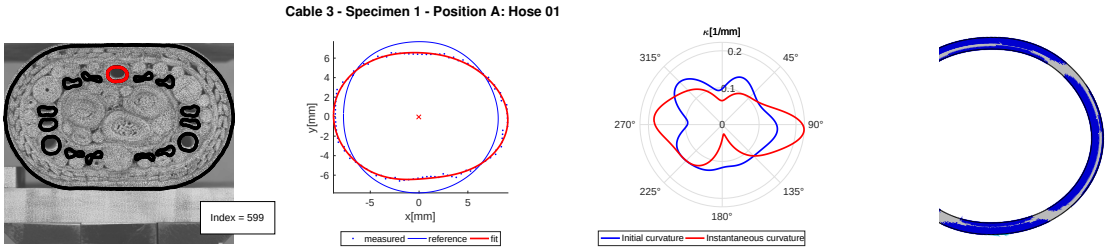

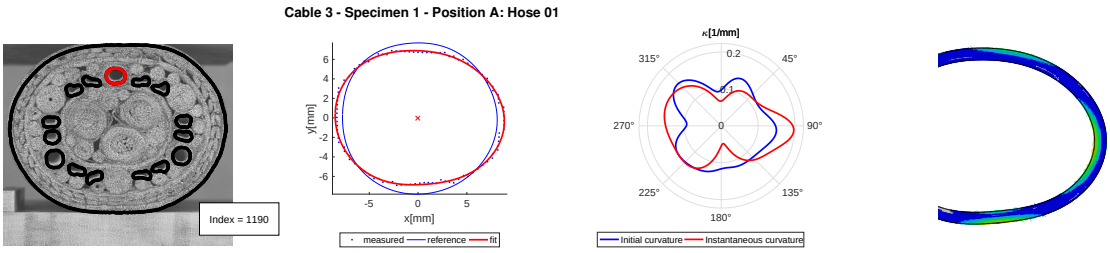

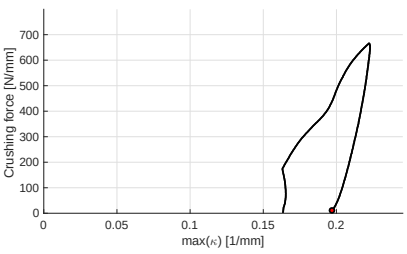

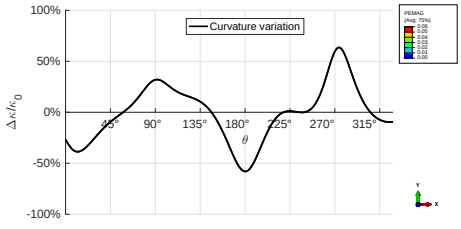

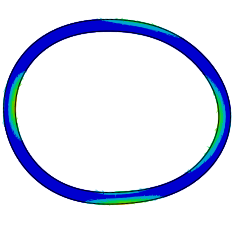

Figure 6.55: Curvature tracking with the DIC system. Test T3-01 with specimen C3-1. Tracking of Hose 08.

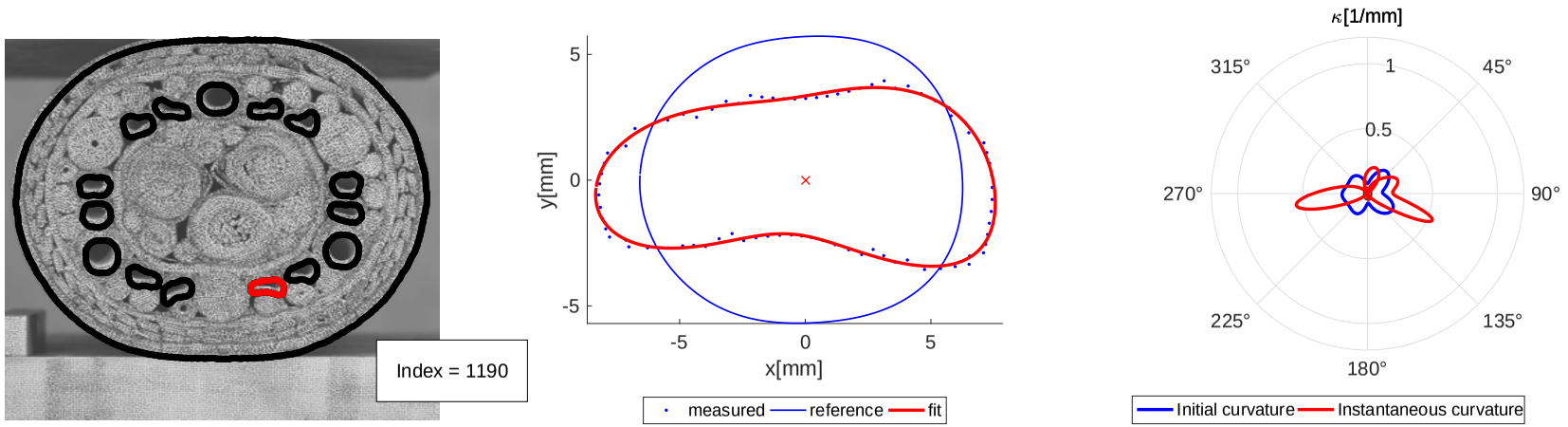

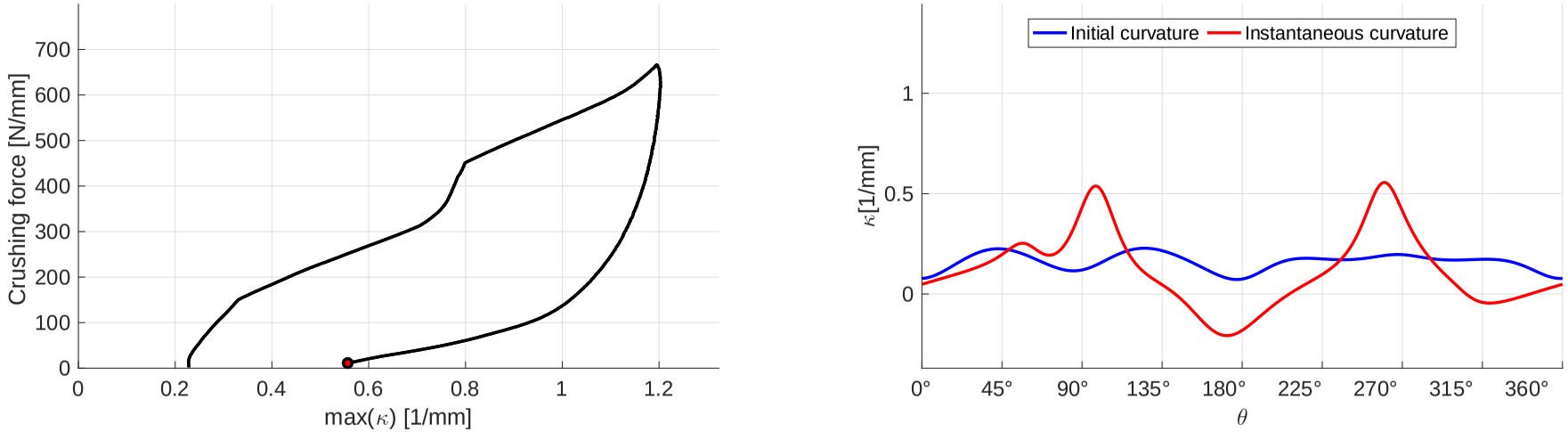

An original analysis methodology for umbilical cables crushing was presented based on numerical models and innovative experimental techniques. The proposed methodology was tested by means of case studies with three umbilicals. If properly implemented, it can certainly represent an important gain in umbilical cables design, analysis and in homologation tests.

The following flowchart in Figure 6.56 summarizes the proposed methodology. During the experimental crushing tests, the profiles of all tubular components are tracked with a DIC system. A curvature calculation methodology is implemented to identify the critical component in the umbilical cross section for each test. This component is monitored individually. The DIC data is then used (a) to evaluate the curvature variation along the tests and (b) as input to a plane strain FEA, which is fed by homologated stress-strain curves in the case of steel tubes and by equivalent ring models (see Appendix D) in the case of HCR hoses. This numerical model makes it possible to evaluate the component's stress field and to associate the raise in curvature with the formation of plastic hinges.

Figure 6.56: Flowchart of the proposed experimental crushing analysis of umbilical cables.

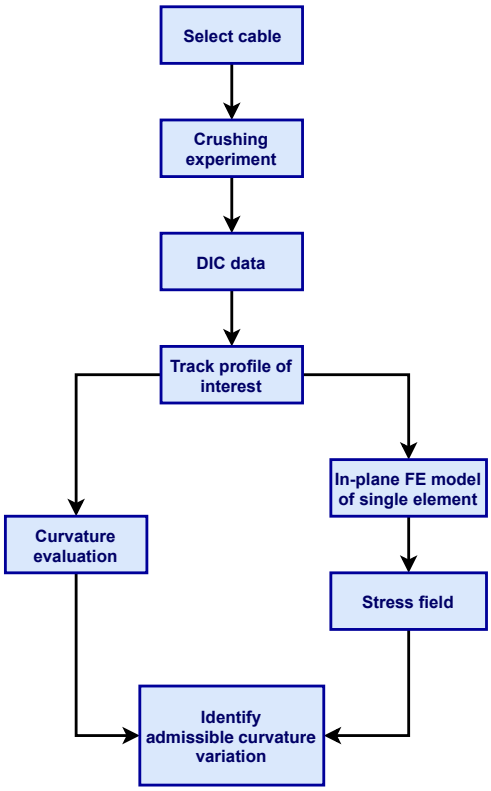

The innovative methodology developed with the DIC system was proven effective. It is the first time that such measurements were made with umbilical cables, providing important information about the behavior of the tubular components when crushed. Such a methodology

enables the calibration of FE crushing models (2D or 3D), providing the umbilical cable designer with valuable analysis tools; it also suggests new homologation tests procedures.

The results obtained in the performed case studies demonstrate that steel tubes and HCR hoses are extremely resistant. It took very high crushing loads to do any significant damage to these components.

The experimental results may provide a better understanding of umbilical cable crushing, as well as of how their internal components may behave when crushed. Even though it was not possible to show what actually occurs along the whole sample, since only the front face of the cross section was visible, the present pioneer experimental DIC system-based assessment still proved to be a powerful method. By indicating how each component may displace during simple crushing tests, the obtained results will certainly promote improvements in FE modeling and design. It is worth remembering that the yield of metallic components and even the formation of plastic hinges do not necessarily mean that the functionality of a tubular component would actually be compromised.

6.6.1 Further work

To improve the innovative methodology, the DIC displacement measurements could be used in a full three-dimensional model of a single component. The current technique employed the optical data to impose displacement in internal nodes of a simple plane strain FE model. The use of a 3D model would increase geometry complexity, particularly in the case of HCR hoses. The analysis of the interlocked profile of the inner metallic carcass could be improved to make the plastic strain evaluation even more reliable.

As in the previous chapter, the main focus of the experimental assessment was the integrity of metallic tubular components. Despite the high deformations suffered by these components, post-crushing inspections of the thermoplastic hoses did not indicate any visible damage. This fact is to be better investigated. Dissection followed by close inspection procedures may further complement failure analysis.

7 CONCLUSIONS

The research presented in this thesis successfully establishes new modeling techniques to deal with the structural analysis of flexible pipes and umbilical cables. Besides the new modeling methodologies, the text also describes a completely novel experimental approach that employs a Digital Image Correlation system to evaluate umbilical cables subjected to crushing loads.

In the first part of the text, which discusses the structural analysis of flexible pipes using mainly FE models, an original modeling technique was established. This technique proposed a bimaterial concept to represent helical layers. Chapter 3 highlighted its advantages and drawbacks making use of three case studies with flexible pipes found in the literature.

The next chapter used this bimaterial concept to model a fourth flexible pipe. In addition to the use of the bimaterial layers, a viscoelastic rheology was considered for the outer plastic sheath and the bending behavior of the numerical pipe model was analyzed. Typical hysteretic bending cycles of flexible pipes were obtained for different coefficients of friction and load rates. This case study allowed the evaluation of the role of viscoelasticity on the bending behavior of a flexible pipe.

The second part of the thesis addressed the structural analysis of umbilical cables subjected to crushing. A two-dimensional modeling methodology of the phenomenon was established and presented. The in-plane modeling took into account a few three-dimensional effects by employing analytical equations. This methodology was tested with three case studies, proving to be reliable and expeditious.

To conclude the crushing analysis, the last chapter presented the development of an experimental crushing campaign using samples of the same three umbilicals from the previous chapter. 2D modeling techniques were adopted to replicate the experimental test conditions and to illustrate once again the modeling reliability presented in the previous chapter.

The crushing tests were monitored with a Digital Image Correlation system, ensuring that profiles of all tubular components were tracked. Displacements were measured and used to calculate curvature variations, allowing to determine the components with higher deformation in each test. The last step of the crushing analysis was the evaluation of stress fields in some critical components, using the data from the optical system as input of a simple plane strain FE model. It was possible to correlate curvature variation with formation of plastic hinges in the analyzed sections.

As a final result from Part II, a novel experimental-numerical methodology for the analysis of umbilical cables subjected to crushing loads was presented. It (a) enables the calibration of FE crushing models (2D or 3D), providing the umbilical cable designer with valuable analysis tools, and (b) suggests new homologation test procedures. The reliability and simplicity of the

equipment and techniques involved make these techniques suitable to be used by the industry for design and certification of umbilical cables.

Lastly, the interested reader is invited to consider further work suggestions, stated in the final remarks sections of Chapters 3, 4, 5 and 6.

REFERENCES

ABAQUS. **ABAQUS Documentation**. Dassault Systèmes, version 6.13-2. [n.p.], 2013.

ARANHA, J. A. P.; MARTINS, C. A.; PESCE, C. P. Analytical approximation for the dynamic bending moment at the touchdown point of a catenary riser. **International Journal of Offshore and Polar Engineering**, International Society of Offshore and Polar Engineers, v. 7, n. 04, p. 8, 1997.

BAHTUI, A.; ALFANO, G.; BAHAI, H. A multi-scale approach to the analysis of ultra deep-water unbonded flexible risers. **Proceedings of the 28th International Conference on Ocean, Offshore and Arctic Engineering, Volume 3: Pipeline and Riser Technology**. pp. 885–891, 2009. DOI: 10.1115/OMAE2009-80182.

BAI, Y.; LU, Y.; CHENG, P. Theoretical and finite-element study of mechanical behaviour of central, large-diameter umbilical cables under tension and torsion. **Ships and Offshore Structures**, Taylor & Francis, v. 10, n. 4, pp. 393–403, 2014. DOI: 10.1080/17445302.2014.938434.

BATHE, K.-J. **Finite element procedures**. Second edition. United States: Prentice Hall, 1996. 1037 pp.

BLANCO, J. A.; COSTELLO, G. A. Cylindrical constraint of helical springs. **Journal of Applied Mechanics**, American Society of Mechanical Engineers, v. 41, n. 4, p. 1138, 1974. DOI: 10.1115/1.3423457.

BOG, T.; ZANDER, N.; RANK, E. Normal contact with high order finite elements and a fictitious contact material. **Computers & Mathematics with Applications**, Pergamon, v. 70, n. 7, pp. 1370–1390, 2015. DOI: 10.1016/J.CAMWA.2015.04.020.

BOOM, H. J. J. van den; DE BOER, G. Damping and hysteresis effects on the behaviour of flexible risers. **Behaviour of Offshore Structures (BOSS)**. p. 22, 1992.

BRINSON, H. F.; BRINSON, L. C. **Polymer engineering science and viscoelasticity**. Boston, MA: Springer US, 2015. DOI: 10.1007/978-1-4899-7485-3.

CAIRE, M.; VAZ, M. A.; LEMOS, C. A. D. Viscoelastic analysis of bend stiffeners. **Proceedings of the 24th International Conference on Offshore Mechanics and Arctic Engineering, Volume 3**. pp. 531–538, 2005. DOI: 10.1115/OMAE2005-67321.

CERFONTAINE, B.; DIEUDONNÉ, A. C.; RADU, J. P.; COLLIN, F.; CHARLIER, R. 3D zero-thickness coupled interface finite element: formulation and application. **Computers and Geotechnics**, Elsevier, v. 69, pp. 124–140, 2015. DOI: 10.1016/J.COMPGEO.2015.04.016.

CHEN, T. **Determining a prony series for a viscoelastic material from time varying strain data**. Hampton, Virginia: NASA (National Aeronautics and Space Administration), 2000. 26 pp.

COOK, R. D.; MALKUS, D. S.; PLESHA, M. E.; WITT, R. J. **Concepts and applications of finite element analysis**. Fourth edition. United States: John Wiley and Sons, 2001. 736 pp.

COSTA, C. H. O. **Correlação analítico - experimental de risers flexíveis sobmetidos a cargas radiais**. 2003. 131 pp. Dissertation (Master) — Universidade Federal do Rio de Janeiro.

COSTELLO, G. A. Large deflections of helical spring due to bending. **Journal of the Engineering Mechanics Division**, v. 103, n. 3, pp. 481–487, 1977.

CRUZ, F. T. L. **Análise estrutural de linhas flexíveis pelo método dos elementos finitos**. 1996. Dissertation (Master) — Universidade de São Paulo.

CUSTÓDIO, A. B.; VAZ, M. A. A nonlinear formulation for the axisymmetric response of umbilical cables and flexible pipes. **Applied Ocean Research**, Elsevier, v. 24, n. 1, pp. 21–29, 2002. DOI: 10.1016/S0141-1187(02)00007-X.

DAI, T.; YE, N.; SÆVIK, S. The effect of stick stiffness of friction models on the bending behavior in non-bonded flexible risers. **Proceedings of the 36th International Conference on Ocean, Offshore and Arctic Engineering, Volume 5A: Pipelines, Risers, and Subsea Systems**. p. V05AT04A041, 2017. DOI: 10.1115/OMAE2017-62644.

DESAI, C. S.; ZAMAN, M. M.; LIGHTNER, J. G.; SIRIWARDANE, H. J. Thin-layer element for interfaces and joints. **International Journal for Numerical and Analytical Methods in Geomechanics**, Wiley-Blackwell, v. 8, n. 1, pp. 19–43, 1984. DOI: 10.1002/nag.1610080103.

DIXON, M. A. J.; ZHAO, T. 3D modeling improves deepwater umbilical design dependability. **Offshore Technology Conference**. 2008. DOI: 10.4043/19513-MS.

DOBSON, A.; PROBYN, I.; MARTINEZ, M.; BORDET, S. Multi-axis finite element analysis of helical umbilical structures in bending, tension and crushing. **Subsea Controls and Data Acquisition 2006: Controlling the Future Subsea**. p. 10, 2006.

FÉRET, J. J.; BOURNAZEL, C. L. Calculation of stresses and slip in structural layers of unbonded flexible pipes. **Journal of Offshore Mechanics and Arctic Engineering**, American Society of Mechanical Engineers, v. 109, n. 3, p. 263, 1987. DOI: 10.1115/1.3257019.

FERGESTAD, D.; LØTVEIT, S. A.(Ed.). **Handbook on design and operation of flexible pipes**. Trondheim, Norway: NTNU, 4Subsea and SINTEF Ocean, 2017. 686 pp.

FERRY, J. D. **Viscoelastic properties of polymers**. Third edition. United States: John Wiley and Sons, 1980. 641 pp.

FLÜGGE, W. **Viscoelasticity**. Berlin, Heidelberg: Springer, 1975. DOI: 10.1007/978-3-662-02276-4.

FRANZINI, G. R.; PESCE, C. P.; TAKAFUJI, F. C. M.; GONÇALVES, R. T.; TANAKA, R. L.; SILVA, M. R.; BARBOSA NETO, T. F.; GODINHO, C. A. F. Crushing of flexible pipes under traction: a theoretical-experimental assessment. **Proceedings of the 30th International Conference on Ocean, Offshore and Arctic Engineering, Volume 4: Pipeline and Riser Technology**. pp. 503–512, 2011. DOI: 10.1115/OMAE2011-49524.

GAY NETO, A.; MARTINS, C. A. A comparative buckling study for the carcass layer of flexible pipes. **Proceedings of the 28th International Conference on Ocean, Offshore and Arctic Engineering, Volume 3: Pipeline and Riser Technology**. pp. 419–428, 2009. DOI: 10.1115/OMAE2009-79507.

GAY NETO, A.; MARTINS, C. A. A comparative wet collapse buckling study for the carcass layer of flexible pipes. **Journal of Offshore Mechanics and Arctic Engineering**, American Society of Mechanical Engineers, v. 134, n. 3, p. 031701, 2012. DOI: 10.1115/1.4005185.

GAY NETO, A.; MARTINS, C. A. Flexible pipes: influence of the pressure armor in the wet collapse resistance. **Journal of Offshore Mechanics and Arctic Engineering**, American Society of Mechanical Engineers, v. 136, n. 3, p. 031401, 2014. DOI: 10.1115/1.4027476.

GAY NETO, A.; MARTINS, C. A.; PESCE, C. P.; BARBOSA NETO, T. F. A numerical simulation of crushing in flexible pipes. **Proceedings of the 20th International Congress of Mechanical Engineering**. p. 10, 2009.

GAY NETO, A.; MARTINS, C. A.; PESCE, C. P.; MEIRELLES, C. O. C.; MALTA, E. R.; BARBOSA NETO, T. F.; GODINHO, C. A. F. Prediction of burst in flexible pipes. **Journal of Offshore Mechanics and Arctic Engineering**, American Society of Mechanical Engineers, v. 135, n. 1, p. 011401, 2013b. DOI: 10.1115/1.4007046.

GREALISH, F.; SMITH, R.; ZIMMERMAN, J. New industry guidelines for fatigue analysis of unbonded flexible risers. **Offshore Technology Conference**. 2006. DOI: 10.4043/18303-MS.

GUTTNER, W. C. **Modelo tridimensional em elementos finitos para a análise de cabo umbilical STU submetido ao carregamento de crushing**. 2015. 163 pp. Dissertation (Master) — Universidade de São Paulo.

GUTTNER, W. C.; SANTOS, C. C. P.; PESCE, C. P. A finite element method assessment of a Steel Tube Umbilical (STU) cable subjected to crushing load: Comparison between two and

three-dimensional approaches. **Marine Structures**, Elsevier, v. 53, pp. 52–67, 2017. DOI: 10.1016/J.MARSTRUC.2017.01.002.

KNAPP, R. H. Derivation of a new stiffness matrix for helically armoured cables considering tension and torsion. **International Journal for Numerical Methods in Engineering**, Wiley-Blackwell, v. 14, n. 4, pp. 515–529, 1979. DOI: 10.1002/nme.1620140405.

LANTEIGNE, J. Theoretical estimation of the response of helically armored cables to tension, torsion, and bending. **Journal of Applied Mechanics**, American Society of Mechanical Engineers, v. 52, n. 2, p. 423, 1985. DOI: 10.1115/1.3169064.

LAVISION. **Digital Image Correlation (DIC)**. Available in: <http://www.lavision.de/en/techniques/dic-dvc/index.php>. Accessed on: May 25, 2017.

LE CORRE, V.; PROBYN, I. Validation of a 3-dimensional finite element analysis model of deep water steel tube umbilical in combined tension and cyclic bending. **Proceedings of the 28th International Conference on Ocean, Offshore and Arctic Engineering, Volume 3: Pipeline and Riser Technology**. pp. 77–86, 2009. DOI: 10.1115/OMAE2009-79168.

LEROY, J.-M.; PERDRIZET, T.; Le Corre, V.; ESTRIER, P. Stress assessment in armour layers of flexible risers. **Proceedings of the 29th International Conference on Ocean, Offshore and Arctic Engineering, Volume 5, Parts A and B**. pp. 951–960, 2010. DOI: 10.1115/OMAE2010-20932.

LOVE, A. E. H. **A treatise on the mathematical theory of elasticity**. Fourth edition. New York: Dover Publications, 1944. 643 pp.

MALTA, E. R. **Investigação do comportamento estrutural de tubos flexíveis sob cargas compressivas**. 2016. 268 pp. Thesis (Doctoral) — Universidade de São Paulo.

MALTA, E. R.; MARTINS, C. A. Finite element analysis of flexible pipes under compression. **Proceedings of the 33rd International Conference on Ocean, Offshore and Arctic Engineering, Volume 6A: Pipeline and Riser Technology**. p. V06AT04A010, 2014. DOI: 10.1115/OMAE2014-23192.

MALTA, E. R.; MARTINS, C. A. Finite element analysis of flexible pipes under axial compression: influence of the sample length. **Journal of Offshore Mechanics and Arctic Engineering**, American Society of Mechanical Engineers, v. 139, n. 1, p. 011701, 2016. DOI: 10.1115/1.4034379.

MALTA, E. R.; MARTINS, C. A.; GONÇALVES, S. H.; GAY NETO, A. Finite element modeling of flexible pipes under crushing loads. **Proceedings of the 32nd International**

Conference on Ocean, Offshore and Arctic Engineering, Volume 4A: Pipeline and Riser Technology. p. V04AT04A030, 2013. DOI: 10.1115/OMAE2013-10307.

MARLOW, R. S. A general first-invariant hyperelastic constitutive model. **Constitutive Models for Rubber**, pp. 157–160, 2003.

MARTINS, C. A.; PESCE, C. P.; ARANHA, J. A. P. **Modelo simplificado de comportamento estrutural sob carregamento localizado pela ação de lagartas de tração durante o lançamento. parte II: efeito do squeezing e carregamento ao longo da linha**. São Paulo: EPUSP/PIRELLI, 1996. 23 pp. TEC 18.01 - Tubo de Produção (Gás Lift) 2"1/2 - 3000psi. (restricted access).

MARTINS, C. A.; PESCE, C. P.; ARANHA, J. A. P. Structural behavior of flexible pipe carcass during launching. **Proceedings of the 22nd International Conference on Offshore Mechanics and Arctic Engineering, Volume 2: Safety and Reliability; Pipeline Technology**. pp. 537–546, 2003. DOI: 10.1115/OMAE2003-37053.

MENDONÇA, H. G. **Análise paramétrica do efeito de cargas de esmagamento e estrangulamento sobre um tubo flexível na operação de lançamento**. 2016. 146 pp. Dissertation (Master) — Universidade de São Paulo.

MERINO, H. E. M.; SOUSA, J. R. M.; MAGLUTA, C.; ROITMAN, N. On the coupled extensional–torsional response of flexible pipes. **Proceedings of the 28th International Conference on Ocean, Offshore and Arctic Engineering, Volume 3: Pipeline and Riser Technology**. pp. 359–371, 2009. DOI: 10.1115/OMAE2009-79468.

MERINO, H. E. M.; SOUSA, J. R. M.; MAGLUTA, C.; ROITMAN, N. Numerical and experimental study of a flexible pipe under torsion. **Proceedings of the 29th International Conference on Ocean, Offshore and Arctic Engineering, Volume 5, Parts A and B**. pp. 911–922, 2010. DOI: 10.1115/OMAE2010-20902.

NOVITSKY, A.; SERTÃ, S. Flexible pipes in brazilian ultra-deepwater fields – a proven solution. **Proceedings of the 14th Deep Offshore Technology, Riser Technology Symposium**. p. 17, 2002.

PÉRONNE, S.; IZARN, C.; ESTRIER, P.; CARO, O.; LEROY, J.-M.; CHARLIAC, D. Flexible pipe hysteretic bending behavior: comparison with experimental characterization and finite element method. **Proceedings of the 34th International Conference on Ocean, Offshore and Arctic Engineering, Volume 5A: Pipeline and Riser Technology**. p. V05AT04A032, 2015. DOI: 10.1115/OMAE2015-41281.

PESCE, C. P. **Mecânica de cabos e tubos submersos lançados em catenária: uma abordagem analítica e experimental**. 1997. Thesis (Doctoral) — Universidade de São Paulo, São Paulo.

PESCE, C. P. **Modelos analíticos em mecânica-estrutural de tubos flexíveis: distribuição de esforços solicitantes em seções de tubos flexíveis: modelos de primeira geração sob tração e flexão**. São Paulo: EPUSP/Prysmian, 2008a. 96 pp. Relatório Técnico SM-05. Tubos Flexíveis – Programas de Desenvolvimento e Qualificação de Protótipos Metodologia de Projeto - FASE 1: Ferramentas Computacionais e Modelos. (restricted access).

PESCE, C. P.; FRANZINI, G. R.; RABELO, M. A.; RAMOS JR., R.; GONÇALVES, R. T.; TANAKA, R. L.; BARBOSA NETO, T. F.; GODINHO, C. A. F. A nonlinear analytical model for flexible pipe crushing analysis. **Proceedings of the 31st International Conference on Ocean, Offshore and Arctic Engineering, Volume 3: Pipeline and Riser Technology**. p. 569, 2012. DOI: 10.1115/OMAE2012-83701.

PESCE, C. P.; FUJARRA, A. L. C.; RABELO, M. A.; TANAKA, R. L.; MARTINS, C. A.; SILVEIRA, L. M. Y. da; BARROS, E. E.; GODINHO, C. A. F. Structural behavior of umbilicals: Part II - Model-experimental comparisons. **Proceedings of the 29th International Conference on Ocean, Offshore and Arctic Engineering, Volume 5, Parts A and B**. pp. 893–898, 2010a. DOI: 10.1115/OMAE2010-20895.

PESCE, C. P.; MARTINS, C. A. Numerical computation of riser dynamics. In: **Numerical Models in Fluid-Structure Interaction**. United States: WIT Press, 2005. v. 18, chap. Chapter 7, pp. 253–309. DOI: 10.2495/978-1-85312-837-0/07.

PESCE, C. P.; MARTINS, C. A.; FUJARRA, A. L. C.; FRANZINI, G. R.; TAKAFUJI, F. C. M. **Modelos analíticos em mecânica-estrutural de tubos flexíveis: rotinas do PipeDesign 1.0**. São Paulo: EPUSP/Prysmian, 2008b. Relatório Técnico SM-07. Tubos Flexíveis – Programas de Desenvolvimento e Qualificação de Protótipos Metodologia de Projeto - FASE 1: Ferramentas Computacionais e Modelos. (restricted access).

PESCE, C. P.; MARTINS, C. A.; GAY NETO, A.; FUJARRA, A. L. C.; TAKAFUJI, F. C. M.; FRANZINI, G. R.; BARBOSA NETO, T. F.; GODINHO, C. A. F. Crushing and wet collapse of flowline carcasses: a theoretical-experimental approach. **Proceedings of the 29th International Conference on Ocean, Offshore and Arctic Engineering, Volume 5, Parts A and B**. pp. 521–529, 2010b. DOI: 10.1115/OMAE2010-20423.

PESCE, C. P.; RAMOS JR., R.; DA SILVEIRA, L. M. Y.; TANAKA, R. L.; MARTINS, C. A.; TAKAFUJI, F. C. M.; NOVAES, J. P. Z.; GODINHO, C. A. F. Structural behavior of umbilicals: Part I - Mathematical modeling. **Proceedings of the 29th International Conference on Ocean, Offshore and Arctic Engineering, Volume 5, Parts A and B**. pp. 871–880, 2010c. DOI: 10.1115/OMAE2010-20892.

PESCE, C. P.; RAMOS JR., R.; MARTINS, C. A.; TAKAFUJI, F. C. M.; TANAKA, R. L. **Análise mecânico-estrutural: modelos de esforços na seção de um cabo umbilical**. São Paulo: FINEP/Prysmian, 2008c. 183 pp. Relatório Técnico 2-02/1 v.3. Estudo e Análise de Nova Geração de Cabos Umbilicais Integrados. Convênio Ref.: 2882/0. (restricted access).

PETROBRAS. **Pré-sal: produção de petróleo e gás natural**. Available in: <http://www.petrobras.com.br/pt/nossas-atividades/areas-de-atuacao/exploracao-e-producao-de-petroleo-e-gas/pre-sal/>. Accessed on: September 26, 2016.

PHILLIPS, J. W.; COSTELLO, G. A. Contact stresses in twisted wire cables. **Journal of the Engineering Mechanics Division**, v. 99, n. 2, pp. 331–341, 1973.

PROBYN, I.; DOBSON, A.; MARTINEZ, M. Advances in 3D FEA techniques for metallic tube umbilicals. **Proceedings of the 17th International Offshore and Polar Engineering**. 2007.

PROVASI, R. **Contribuição ao projeto de cabos umbilicais e tubos flexíveis: ferramentas de CAD e modelo de macro elementos**. 2013. 291 pp. Thesis (Doctoral) — Universidade de São Paulo, São Paulo. DOI: 10.11606/T.3.2012.tde-29072013-120723.

PRYSMIAN. **Subsea umbilicals, risers & flowlines (SURF)**. Available in: <https://www.prysmiangroup.com/en/stories/projects-and-business/oil-and-gas/subsea-umbilicals-risers-and-flowlines-surf>. Accessed on: September 26, 2016.

RABELO, M. A. **Investigação sobre a instabilidade axissimétrica de tubos de polietileno de alta densidade sujeitos a compressão axial e pressurização interna e um critério de previsão do fenômeno de 'birdcaging' em tubos flexíveis**. 2014. 288 pp. Thesis (Doctoral) — Universidade de São Paulo, São Paulo. DOI: 10.11606/T.3.2014.tde-26082015-102250.

RABELO, M. A.; PESCE, C. P.; SANTOS, C. C. P.; RAMOS JR., R.; FRANZINI, G. R.; GAY NETO, A. An investigation on flexible pipes birdcaging triggering. **Marine Structures**, Elsevier, v. 40, pp. 159–182, 2015. DOI: 10.1016/J.MARSTRUC.2014.10.010.

RAMOS JR., R. **Modelos analíticos no estudo do comportamento estrutural de tubos flexíveis e cabos umbilicais**. 2001. 396 pp. Thesis (Doctoral) — Universidade de São Paulo.

RAMOS JR., R.; KAWANO, A. Local structural analysis of flexible pipes subjected to traction, torsion and pressure loads. **Marine Structures**, Elsevier, v. 42, pp. 95–114, 2015. DOI: 10.1016/J.MARSTRUC.2015.03.004.

RAMOS JR., R.; MARTINS, C. A.; PESCE, C. P.; ROVERI, F. E. A case study on the axial-torsional behavior of flexible risers. **Proceedings of the 27th International Conference on Offshore Mechanics and Arctic Engineering, Volume 3: Pipeline and Riser Technology; Ocean Space Utilization**. pp. 481–491, 2008. DOI: 10.1115/OMAE2008-57514.

RAMOS JR., R.; MARTINS, C. A.; PESCE, C. P.; ROVERI, F. E. Some further studies on the axial–torsional behavior of flexible risers. **Journal of Offshore Mechanics and Arctic**

Engineering, American Society of Mechanical Engineers, v. 136, n. 1, p. 011701, 2014. DOI: 10.1115/1.4025541.

RAMOS JR., R.; PESCE, C. P. A stability analysis of risers subjected to dynamic compression coupled with twisting. **Journal of Offshore Mechanics and Arctic Engineering**, American Society of Mechanical Engineers, v. 125, n. 3, p. 183, 2003. DOI: 10.1115/1.1576819.

RAMOS JR., R.; PESCE, C. P. A consistent analytical model to predict the structural behavior of flexible risers subjected to combined loads. **Journal of Offshore Mechanics and Arctic Engineering**, American Society of Mechanical Engineers, v. 126, n. 2, p. 141, 2004. DOI: 10.1115/1.1710869.

ROYLANCE, D. **Engineering viscoelasticity**. Cambridge, MA: Department of Materials Science and Engineering, Massachusetts Institute of Technology, 2001. 37 pp.

SÆVIK, S. A finite element model for predicting stresses and slip in flexible pipe armouring tendons. **Computers & Structures**, Pergamon, v. 46, n. 2, pp. 219–230, 1993. DOI: 10.1016/0045-7949(93)90187-I.

SÆVIK, S. Theoretical and experimental studies of stresses in flexible pipes. **Computers & Structures**, Pergamon, v. 89, n. 23-24, pp. 2273–2291, 2011. DOI: 10.1016/J.COMPSTRUC.2011.08.008.

SÆVIK, S.; BRUASETH, S. Theoretical and experimental studies of the axisymmetric behaviour of complex umbilical cross-sections. **Applied Ocean Research**, Elsevier, v. 27, n. 2, pp. 97–106, 2005. DOI: 10.1016/J.APOR.2005.11.001.

SÆVIK, S.; GJØSTEEN, J. K. Ø. Strength analysis modelling of flexible umbilical members for marine structures. **Journal of Applied Mathematics**, Hindawi, v. 2012, pp. 1–18, 2012. DOI: 10.1155/2012/985349.

SANTOS, C. C. P. **Modelo estrutural em elementos finitos de um tubo flexível sob esforços axissimétricos e de flexão**. São Paulo: Final graduation work report – Universidade de São Paulo, 2013. 86 pp.

SANTOS, C. C. P.; PESCE, C. P.; FRANZINI, G. R.; OTTE FILHO, O. O. An experimental assessment on umbilical cable crushing using digital image correlation. **Proceedings of the 35th International Conference on Ocean, Offshore and Arctic Engineering, Volume 5: Pipelines, Risers, and Subsea Systems**. p. V005T04A017, 2016. DOI: 10.1115/OMAE2016-54875.

SANTOS, C. C. P.; PESCE, C. P.; RABELO, M. A.; RAMOS JR., R. An assessment of HDPE viscoelastic behavior effects on the bending of offshore flexible pipes. **Proceedings of the 23rd ABCM International Congress of Mechanical Engineering (COBEM2015)**. p. 10, 2015a. DOI: 10.20906/CPS/COB-2015-1469.

SANTOS, C. C. P.; PESCE, C. P.; RAMOS JR., R. An alternative strategy for offshore flexible pipes finite element analysis. **Conference on Advances in Composite Materials and Structures**. 2015b.

SANTOS, C. C. P.; PESCE, C. P.; SALLES, R.; FRANZINI, G. R.; TANAKA, R. L. A finite element model for umbilical cable crushing analysis. **Proceedings of the 34th International Conference on Ocean, Offshore and Arctic Engineering, Volume 5A: Pipeline and Riser Technology**. p. V05AT04A043, 2015c. DOI: 10.1115/OMAE2015-41622.

ScoreSubsea. **Parker Parflex Products**. Available in: <http://www.subsea-wellhead.com/parker-products/parker-parflex-products.php>. Accessed on: September 16, 2016.

SHARMA, K. G.; DESAI, C. S. Analysis and implementation of thin-layer element for interfaces and joints. **Journal of Engineering Mechanics**, v. 118, n. 12, pp. 2442–2462, 1992. DOI: 10.1061/(ASCE)0733-9399(1992)118:12(2442).

SMITH, R.; O'BRIEN, P.; O'SULLIVAN, T.; WEIBE, C. Fatigue analysis of unbonded flexible risers with irregular seas and hysteresis. **Offshore Technology Conference**. 2007. DOI: 10.4043/18905-MS.

SOUSA, J. R. M. **Análise local de linhas flexíveis pelo método dos elementos finitos**. 2005. 809 pp. Thesis (Doctoral) — Universidade Federal do Rio de Janeiro.

SOUSA, J. R. M.; ELLWANGER, G. B.; LIMA, E. C. P.; PAPALEO, A. An analytical model to predict the local mechanical behaviour of flexible risers subjected to crushing loads. **Jornadas Sul-Americanas de Engenharia Estrutural**. p. 18, 2002.

SOUSA, J. R. M.; MAGLUTA, C.; ROITMAN, N.; LONDOÑO, T. V.; CAMPELLO, G. C. A study on the response of a flexible pipe to combined axisymmetric loads. **Proceedings of the 32nd International Conference on Ocean, Offshore and Arctic Engineering, Volume 4B: Pipeline and Riser Technology**. p. V04BT04A040, 2013. DOI: 10.1115/OMAE2013-11384.

SOUSA, J. R. M.; MAGLUTA, C.; ROITMAN, N.; CAMPELLO, G. C. Bending analysis of a flexible pipe with broken tensile armor wires. **Proceedings of the 34th International Conference on Ocean, Offshore and Arctic Engineering, Volume 5A: Pipeline and Riser Technology**. p. V05AT04A038, 2015. DOI: 10.1115/OMAE2015-41436.

SOUSA, J. R. M.; PINHO, A. N.; ELLWANGER, G. B.; LIMA, E. C. P. Numerical analysis of a flexible pipe with damaged tensile armor wires. **Proceedings of the 28th International Conference on Ocean, Offshore and Arctic Engineering, Volume 3: Pipeline and Riser Technology**. pp. 829–839, 2009. DOI: 10.1115/OMAE2009-80014.

SOUSA, J. R. M.; VIERO, P. F.; MAGLUTA, C.; ROITMAN, N. An experimental and numerical study on the axial compression response of flexible pipes. **Journal of Offshore**

Mechanics and Arctic Engineering, American Society of Mechanical Engineers, v. 134, n. 3, p. 031703, 2012. DOI: 10.1115/1.4005181.

SUTTON, M. A.; ORTEU, J.-J.; SCHREIER, H. W. **Image correlation for shape, motion and deformation measurements: basic concepts, theory and applications**. First edition. Boston, MA: Springer US, 2009. 322 pp. DOI: 10.1007/978-0-387-78747-3.

TAN, Z.; QUIGGIN, P.; SHELDRAKE, T. Time domain simulation of the 3d bending hysteresis behaviour of an unbonded flexible riser. **Proceedings of the 26th International Conference on Offshore Mechanics and Arctic Engineering, Volume 3: Pipeline and Riser Technology; CFD and VIV**. pp. 307–314, 2007. DOI: 10.1115/OMAE2007-29315.

TECHNIP. **Flexible pipes**. Available in: <http://www.technip.com/sites/default/files/technip/page/attachments/flexiblepipebrochure.pdf>. Accessed on: September 26, 2016.

TIMOSHENKO, S.; GERE, J. M. **Theory of elastic stability**. Second edition. United States: Dover Publications, 2009. 280 pp.

TORRES, L. C. A. R. **Modelagem viscoelástica não linear de enrijecedores à flexão**. 2014. Thesis (Doctoral) — Universidade Federal do Rio de Janeiro.

VAZ, M. A.; CAIRE, M. On the large deflections of linear viscoelastic beams. **International Journal of Non-Linear Mechanics**, Pergamon, v. 45, n. 1, pp. 75–81, 2010. DOI: 10.1016/J.IJNONLINMEC.2009.09.004.

VAZ, M. A.; CAIRE, M.; GÓMEZ, A. A.; FARIAS, L. F. A. Bend stiffner linear viscoelastic response subjected to harmonic loading. **Proceedings of the 20th International Congress of Mechanical Engineering**. p. 9, 2009.

WANG, X.; WANG, L. B. Continuous interface elements subject to large shear deformations. **International Journal of Geomechanics**, v. 6, n. 2, pp. 97–107, 2006. DOI: 10.1061/(ASCE)1532-3641(2006)6:2(97).

WITZ, J. A. A case study in the cross-section analysis of flexible risers. **Marine Structures**, Elsevier, v. 9, n. 9, pp. 885–904, 1996. DOI: 10.1016/0951-8339(95)00035-6.

WITZ, J. A.; TAN, Z. On the axial-torsional structural behaviour of flexible pipes, umbilicals and marine cables. **Marine Structures**, Elsevier, v. 5, n. 2-3, pp. 205–227, 1992a. DOI: 10.1016/0951-8339(92)90029-O.

WITZ, J. A.; TAN, Z. On the flexural structural behaviour of flexible pipes, umbilicals and marine cables. **Marine Structures**, Elsevier, v. 5, n. 2-3, pp. 229–249, 1992b. DOI: 10.1016/0951-8339(92)90030-S.

WITZ, J. A.; TAN, Z. Rotary bending of marine cables and umbilicals. **Engineering Structures**, Elsevier, v. 17, n. 4, pp. 267–275, 1995. DOI: 10.1016/0141-0296(95)00025-3.

WRIGGERS, P. **Computational contact mechanics**. Berlin, Heidelberg: Springer, 2006. DOI: 10.1007/978-3-540-32609-0.

WRIGGERS, P. **Nonlinear finite element methods**. Berlin, Heidelberg: Springer, 2008. 559 pp. DOI: 10.1007/978-3-540-71001-1.

WRIGGERS, P.; SCHRÖDER, J.; SCHWARZ, A. A finite element method for contact using a third medium. **Computational Mechanics**, Springer Berlin Heidelberg, v. 52, n. 4, pp. 837–847, 2013. DOI: 10.1007/s00466-013-0848-5.

ZHANG, M.; CHEN, X.; FU, S.; GUO, Y.; MA, L. Theoretical and numerical analysis of bending behavior of unbonded flexible risers. **Marine Structures**, Elsevier, v. 44, pp. 311–325, 2015. DOI: 10.1016/J.MARSTRUC.2015.10.001.

APPENDIX A – Viscoelasticity

Several polymers have substantial energy absorption abilities due to their viscoelastic behavior. This category of material is commonly incorporated in mechanical systems to dissipate energy and thus avoid structural damages. Viscoelasticity has been widely studied for decades; Flügge (1975), Ferry (1980), Roylance (2001) and Brinson and Brinson (2015). This material behavior is characterized by a strain time-rate dependence. Structures composed of viscoelastic materials are characterized by a time-delayed response (the force precedes the displacement response), which can be described by a relaxation function and a creep function.

In the offshore scenario, viscoelastic material has been studied in several applications; Caire, Vaz and Lemos (2005), Vaz et al. (2009), Vaz and Caire (2010) and Torres (2014). High-density polyethylene (HDPE), often used for the external layer of flexible pipes, is a typical viscoelastic polymer. Based on Chen (2000), Rabelo (2014) experimentally characterized a HDPE pipe's material behavior through relaxation and creep tests, at different load rates.

A well-known analytical model used to represent linear viscoelastic behavior is the one given by the Prony series, presented in Equation (A.1).

$$P(t) = \sum_{i=1}^{N} \alpha_i . \exp\left(\frac{-t}{\tau_i}\right) \tag{A.1}$$

Considering the strain history, the time dependent stress-strain state of the linear viscoelastic material can be determined. The load and displacement history, which includes the loading time rate, influences the material behavior. The Prony series introduces these dependencies in the constitutive equation. The linear viscoelastic constitutive law used to model the HDPE can be represented by a simple physical arrangement composed of a spring and a damper. The spring is the linear-elastic component and its constitutive equation is Hooke's law, presented in Equation (A.2).

$$\sigma = E.\varepsilon \tag{A.2}$$

The damper introduces the viscous behavior, and its constitutive equation may be written in the form of Equation (A.3), where η is the viscosity constant.

$$\sigma = \eta . \frac{\partial \varepsilon}{\partial t} \tag{A.3}$$

A linear viscoelastic constitutive model may be constructed by superimposing the effects of Equations (A.2) and (A.3). Using the Prony series for the relaxation behavior, a constitutive

relation can be written as follows in Equation (A.4), with $Y(t)$ being the relaxation function.

$$\sigma(t) = Y(t).\varepsilon_0 \tag{A.4}$$

This relaxation function $Y(t)$ is typically modeled with the Prony series as presented in Equation (A.5), where p_i is the i'th Prony constant, τ_i is the i'th Prony delay constant, and E_0 is the initial value of the elastic modulus of the material. It is easily seen that $Y(0) = E_0$ and $Y(\infty) = E_0.(1 - \sum p_i)$.

$$\frac{Y(t)}{E_0} = 1 - \sum_{i=1}^{n} p_i.\left(1 - \exp\left(\frac{-t}{\tau_i}\right)\right) \tag{A.5}$$

This linear viscoelastic approach is used in Chapter 4 to model the external sheath of a flexible pipe.

APPENDIX B – Adopted conventions

This appendix details the conventions adopted for the helical components. Figure B.1 shows two wires helically wound around a cylinder. This image also indicates the Cartesian coordinate system designated by the X, Y and Z-axis, where Z is the axial direction of the cylinder.

Concerning loads and twisting around the Z-axis, counterclockwise rotations observed from the end portion ($z = L$) of the model are considered positive (Figure B.2). From Figure B.1, with a positive imposed torque, the blue wire is pulled while the red wire is compressed.

Figure B.2 also defines the laying angle of the helical layers. This is the angle between a wound wire and the direction of the Z-axis. In Figure B.1, the red wire has a positive laying angle and the blue wire has a negative laying angle.

Figure B.1: Wires helically wound in opposite directions around a core.

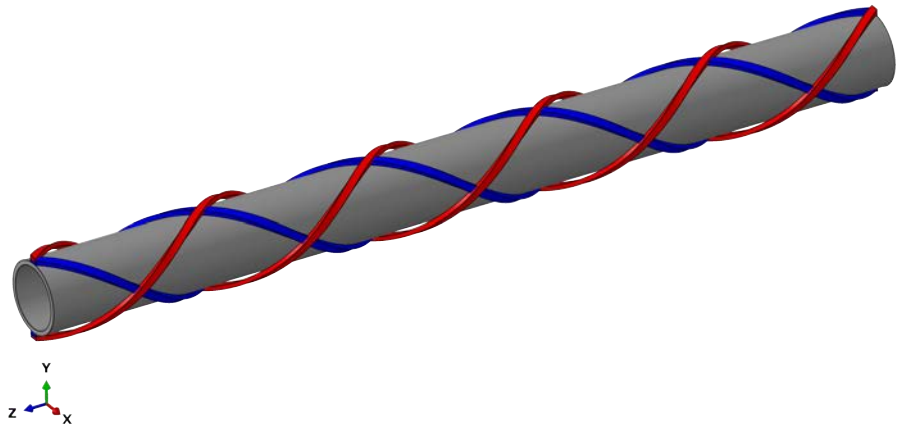

Figure B.2: Positive laying angle α induces positive torque in the counterclockwise sense.

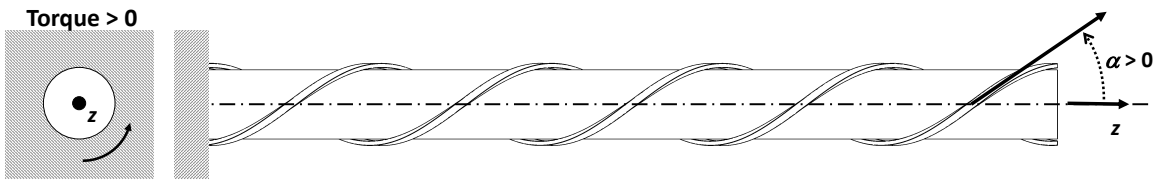

APPENDIX C – Incompatible mode elements

This appendix, completely based on information found in the ABAQUS (2013) documentation, explains the choice for incompatible mode elements when modeling flexible pipe layers with one element through the thickness. At the end, two examples quantify the influence of (a) order of the element (linear or quadratic), (b) element formulation and (c) level of integration, always considering solid three-dimensional elements.

Firstly, consider a fragment of a structure subjected to pure bending. Figure C.1 illustrates its deformation. The horizontal lines take on constant curvature, while the lines through the thickness remain straight. The angles between the lines remain at $90°$, indicating the absence of shear stress.

Figure C.1: Deformation of material subjected to bending moment M.

Source: ABAQUS (2013) documentation.

Nevertheless, the edges of a linear Finite Element do not curve. A linear Finite Element with full-integration subjected to a bending load deforms as illustrated in Figure C.2. For visualization, the dotted lines go through the integration points. Assuming a small displacement, the vertical lines do not change their length, indicating zero stress in direction 2 ($\sigma_{22} = 0$). In the horizontal direction, the horizontal upper line increases ($\sigma_{11} > 0$) and the lower line decreases ($\sigma_{11} < 0$). Also, the angle between horizontal and vertical lines changes, indicating incorrectly a nonzero shear stress ($\sigma_{12} \neq 0$).

Figure C.2: Deformation of a fully integrated, linear element subjected to bending moment M.

Source: ABAQUS (2013) documentation.

The cause of this fake shear stress is that the edges of the linear Finite Element cannot bend. Therefore, the strain energy is creating shearing rather than bending and the deflections are underestimated. The Finite Element remains too stiff in bending, due to an effect known as shear locking, which affects only the performance of linear elements with full-integration. Quadratic elements do not present this problem, since their edges can be curved (Figure C.3).

Figure C.3: Deformation of a fully integrated, quadratic element subjected to bending moment M.

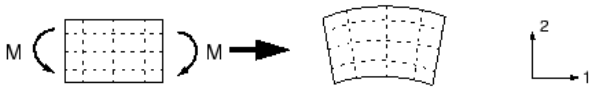

Source: ABAQUS (2013) documentation.

On the other hand, linear elements with reduced integration tend to be too flexible, because of another numerical problem called *hourglassing*. Figure C.4 illustrates again a linear Finite Element subjected to bending, but with only one integration point (reduced integration). Notice that the dotted lines do not change in length, which means that all stress components at the single integration point are zero. The element does not resist to bending since this deformation mode does not generate strain energy, producing meaningless results.

Figure C.4: Deformation of a linear element with reduced integration subjected to bending moment M.

Source: ABAQUS (2013) documentation.

The incompatible mode elements are used to overcome these numerical problems. In regular displacement elements, the linear variation of the axial stress due to bending is accompanied by a linear variation of the stress perpendicular to the bending direction, which leads to incorrect nonzero shear stresses and an overestimation of the stiffness. The incompatible modes prevent such a stress from occurring. They add degrees of freedom to the first-order element, allowing it to present a linear variation of the deformation gradient (Figure C.5). This eliminates the nonzero shear stress.

Figure C.5: Variation of deformation gradient in (a) an incompatible mode (enhanced deformation gradient) element and (b) a first-order element using a standard formulation.

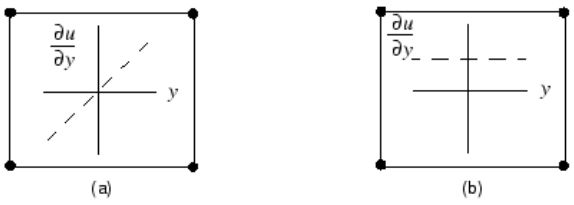

Source: ABAQUS (2013) documentation.

Incompatible mode elements can produce results in bending problems that are comparable to quadratic elements but at significantly lower computational cost. Two examples extracted from ABAQUS (2013) documentation are briefly presented to quantify the performance of solid

elements under bending conditions. Both examples corroborate the choice for incompatible mode elements, once the layers of the flexible pipes modeled have only one element through the thickness. It is shown that, even with fewer degrees of freedom, the incompatible mode elements provide comparably accurate results with respect to the second-order elements.

The following Finite Element types are investigated (presenting the ABAQUS nomenclature):

- **C3D8:** 8-node linear solid element, with full-integration;
- **C3D8I:** 8-node linear solid element, with full-integration and incompatible modes;
- **C3D8R:** 8-node linear solid element, with reduced-integration;
- **C3D20:** 20-node quadratic solid element, with full-integration.

CANTILEVER BEAM WITH END SHEAR LOAD

This first example considers a linear static analysis of a cantilever beam with an end shear load. The Young's modulus used is $E = 689.5GPa$ $(10 \times 10^7 lb/in^2)$, and Poisson's ratio is $\nu = 0$. Load and geometries are presented in Figure C.6, as well as a typical mesh considering 4 elements along the beam and 2 elements through the thickness. The Finite Element analyses were conducted considering the following four mesh sizes: 1, 2, 4, or 8 elements through the thickness, combined with 4 or 16 elements along the length.

Figure C.6: Typical mesh and loading.

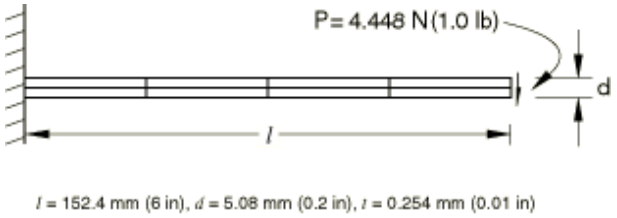

l = 152.4 mm (6 in), d = 5.08 mm (0.2 in), t = 0.254 mm (0.01 in)

Source: ABAQUS (2013) documentation.

The deflection at the end of the beam is predicted as $w_{exact} = 2.74mm$ $(0.108in)$, considering the Euler-Bernoulli beam theory. Regarding only the solid Finite Elements listed above, the numerical results were normalized with respect to the analytical solution and are presented in Table C.1.

The second-order mesh (C3D20) has excellent results, even with the coarse mesh (1x4). The incompatible mode elements (C3D8I) also perform well, even with one element through the beam thickness, indicating their excellent bending properties. On the other hand, the reduced-integration elements (C3D8R) do not resist to bending. With the one-layer mesh,

Table C.1 : Normalized tip deflection of a cantilever beam (w_{fem}/w_{exact}).

Element Type	Mesh Size (Depth x Length)			
	1 x 4	2 x 4	4 x 4	8 x 16
C3D8I	0.985	0.985	0.985	1.000
C3D8	0.035	0.034	0.034	0.364
C3D8R	*	1.306	1.050	1.016
C3D20	0.987	0.987	0.988	1.000

** singular stiffness matrix (no stiffness to resist the bending load)*

Source: Adapted from ABAQUS (2013) documentation.

the beam does not present bending stiffness. With more elements through the thickness, the result converges to the analytical estimation. For the full-integration linear elements (C3D8), the shear-locking causes considerable increase of the beam's bending stiffness, as expected.

BUCKLING ANALYSIS OF RING UNDER EXTERNAL PRESSURE

The second example is the buckling analysis of a ring under external pressure. This tubular geometry is more similar to the conditions found in the flexible pipe models. Figure C.7 presents the geometry and material parameters.

Figure C.7: Ring buckling problem.

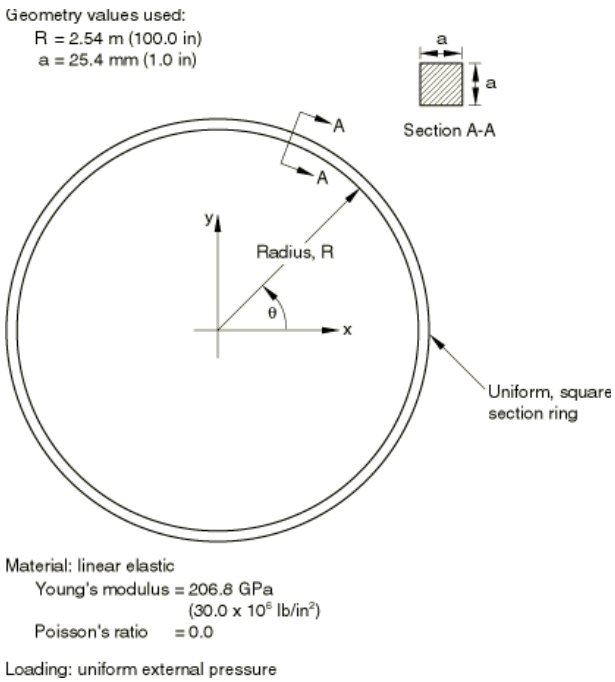

Source: ABAQUS (2013) documentation.

The exact solution to this problem is a critical pressure of $3EI/R^3$, where E is Young's modulus, I is the moment of inertia of the ring, and R is the mean radius. For the parameters presented, the critical pressure is $p_{exact} = 51.71KPa\ (7.5lb/in^2)$. Considering a mesh with 4 elements through the thickness and 80 or 160 elements along the perimeter, Table C.2 presents the normalized pressures calculated with the Finite Element models to reproduce the primary buckling mode, with various types of solid elements.

Table C.2 : Normalized eigenvalue pressure estimates (p_{fem}/p_{exact}). Bernoulli-Euler theory prediction: $p_{exact} = 51.71KPa\ (7.5lb/in^2)$.

Element Type	Mesh Size (Thickness x Perimeter)	
	1 x 4	2 x 4
C3D8I	1.005	1.001
C3D8	31.980	8.700
C3D8R	1.043	0.966
C3D20	1.027	1.002

Source: Adapted from ABAQUS (2013) documentation.

As expected, again the linear full-integration element (C3D8) presents extremely stiff results. Both the incompatible mode (C3D8I) and the second-order elements (C3D20) show excellent results. The reduced-integration elements (C3D8R) with 4 elements through the thickness present acceptable results, floating about the correct value: higher for the coarse mesh and lower for the fine mesh.

Considering that the layers of the Finite Element flexible pipe models have only one element through the thickness, the incompatible mode elements are the best fit for the task.

APPENDIX D – Reinforced hoses as equivalent pipes

The crushing analysis of one isolated hose was performed in order to ensure its relevant crushing behavior. A geometrical simplification of the internal carcass layer was conducted. The interlocked geometry was replaced by an equivalent-thickness pipe, preserving the radial stiffness of the assembly. The original concept, described in detail by Pesce et al. (2010a) and Martins, Pesce and Aranha (2003), is based on usual hypotheses of the linear theory of elastic structures. That model has been extended further to consider plastic deformations, as presented in Pesce et al. (2012).

The basic concept consists in determining the thickness of an equivalent tube with the same stiffness to radial loads (preserving the original flexural modulus of the structure). The flexural modulus per unit of length, D, for the equivalent pipe representing the metallic carcass, can be calculated as follows in Equation (D.1):

$$D = \frac{E.t^3}{12\left(1-\nu^2\right)} = E.\psi.\frac{I^*_{min}}{b} \tag{D.1}$$

The equivalent bending stiffness is related to the minimum principal moment of inertia I^*_{min} of the helically wound section, multiplied by the geometric coverage factor ψ related to the winding process. From Equation (D.1), the equivalent thickness t can be calculated as a function of the metallic carcass parameters:

$$t = \left[12\left(1-\nu^2\right)\psi\frac{I^*_{min}}{b}\right]^{1/3} \tag{D.2}$$

Pesce et al. (2010a) indicates that a correction methodology must be adopted in Equation (D.2), which is represented by a single parameter K. This empirically-defined parameter is meant to account for the loss of flexural stiffness due to the helical geometry. It is introduced in Equation (D.3).

$$t = \left[12\left(1-\nu^2\right)\psi K\frac{I^*_{min}}{b}\right]^{1/3} \tag{D.3}$$

The parameter K may be determined through the same methodology described by Pesce et al. (2010a). This could be done by comparing the linear model results with experimental data, obtained from simple crushing experiments. In the case of interlocked carcasses of flexible pipe, Pesce et al. (2010a) calculate an average value around 0.5 for the K parameter. Instead of conducting specific experiments for the reinforced hoses, we opt to rely on an assumed similarity with interlocked carcasses of flexible pipes and use $K = 0.5$. In fact, this hypothesis has been verified as quite reasonable, as the results below will show.

The second important simplification concerns the representation of the aramid layer. The performance of this layer is negligible during the crushing of the hose. Nevertheless, during the umbilical cable's transportation and installation, the hoses are pressurized in order to protect these tubular components. Therefore, the aramid layer is represented by truss elements in the two-dimensional model, simulating a membrane behavior. Based on linear expansion tests and volumetric expansion tests, the properties of the truss elements were fitted to have a compatible behavior when an internal pressure is applied. Figure D.1 illustrates the red truss elements between the gray and the green elements.

Figure D.1: Reinforced hose finite element mesh.

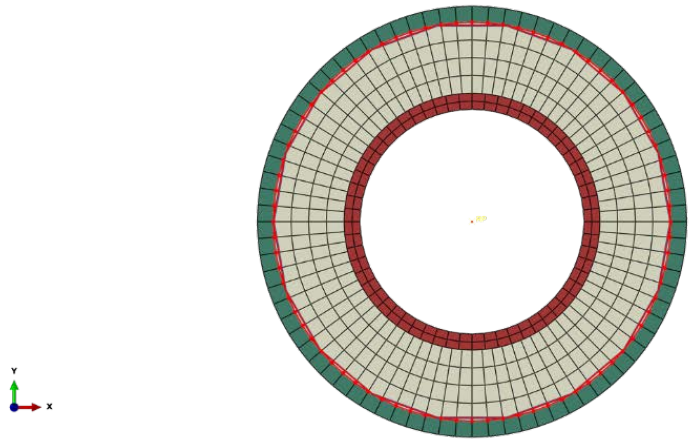

The equivalent tube is represented by the red mesh. The image also illustrates a PA11 layer (gray) and the hose coating (green), represented in the two-dimensional finite model by one single mesh. Each element is assigned the respective material properties.

The equivalent internal tube (ring) is assigned the properties of a 304L stainless steel. An elastic-plastic material behavior is considered, using the classic Ramberg-Osgood fitting function for the hardening due to plastic strain. Such fitting function is the same used by Pesce et al. (2012), Figure (D.2). For the PA11, a hyperelastic behavior is considered, based on Marlow (2003) and using available data from the literature.

Figure (D.3) illustrates the structural response of the equivalent two-dimensional reinforced hose model crushed by two planar shoes. These rigid surfaces have been inputted to simulate the crushing condition of one single reinforced hose. The numerical results are compared with experimental data. Usually, the two-dimensional model returns the shoe force per unit of length. In the present case a $50mm$ length is considered, the same used in the experimental test. That length corresponds to more than 10 carcass pitches.

In the initial range, the resulting curves show a good correlation. The finite element model approximates the radial stiffness quite well. In the plastic regime, the two-dimensional model is conservative up to $10mm$ of displacement. It is noticeable that the inflection of the numerical

Figure D.2: Ramberg-Osgood fitting function used to represent the 304L stainless steel behavior.

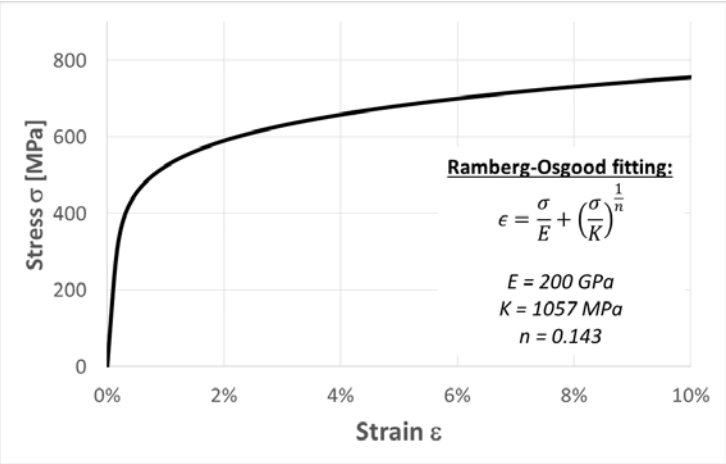

Source: Material parameters from the Offshore Mechanics Laboratory (LMO) database.

Figure D.3: Result for the crushing of a single reinforced hose.

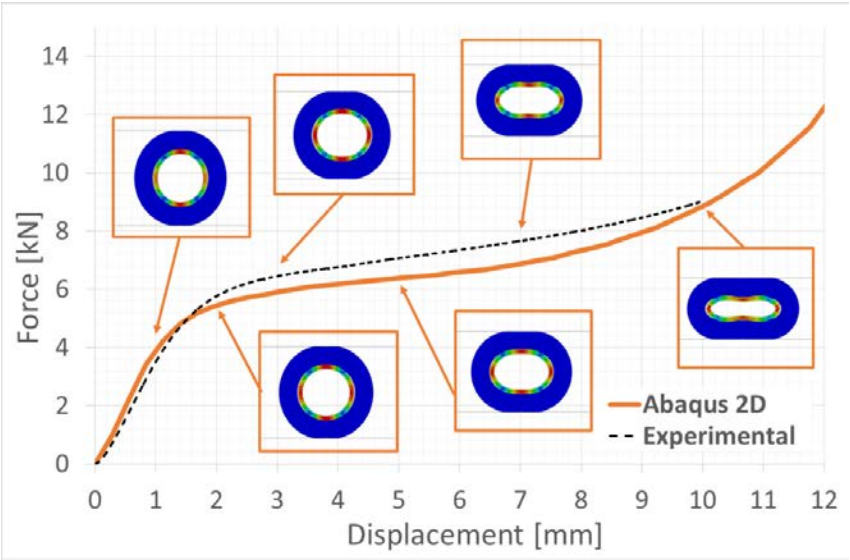

model curve, which is associated with geometrical nonlinearities, is more accentuated than the experimental one.

Concerning the integrity of the HCR hoses, it is not desirable that the numerical analysis reaches such plastic strains compromising the components of the umbilical cross-section. However, this simulation of one single reinforced hose followed by the experimental data comparison provides sufficient evidence of how reliable the two-dimensional model is, ensuring its suitability for the complete umbilical section analysis.